NUMERICAL SIMULATIONS AND CHARACTERIZATION OF THERMALLY DRIVEN FLOWS ON THE MICROSCALE

A Thesis

Submitted to the Faculty

of

Purdue University

by

Aaron Pikus

In Partial Fulfillment of the

Requirements for the Degree

of

Masters in Aerospace Engineering

May 2019

Purdue University

West Lafayette, Indiana

THE PURDUE UNIVERSITY GRADUATE SCHOOL
STATEMENT OF THESIS APPROVAL

Dr. Alina A. Alexeenko, Chair

School of Aeronautics and Astronautics

Dr. Henry J. Melosh

School of Earth, Atmospheric, and Planetary Sciences

Dr. James Poggie

School of Aeronautics and Astronautics

Approved by:

Dr. Weinong Wayne Chen

Head of the School of Aeronautics and Astronautics Graduate Program

ACKNOWLEDGMENTS

I would like to acknowledge Professor Alexeenko first and foremost for her mentorship, guidance, and support. We first met when I was a high school senior visiting Purdue, and she has mentored me ever since by allowing me to join her research group as a freshmen. I definitely learned a lot from her through all the projects we've worked on, including research projects and school projects such as Hyperloop and SASSI2. However, the conversations I most appreciate are the ones we had that aren't directly related to a particular project, but those where we talked about current or historical events in the aerospace world, or even my career options.

I also would like to acknowledge Professor Melosh, who has been a great mentor for me ever since I started graduate school. He has introduced me to a new area of research and broadened my experience greatly. I also enjoyed our many conversations that were unrelated to my research.

I owe a great thanks for Dr. Israel Sebastião, who volunteered his time to mentor me as an undergraduate student. Without him, I would not have been able to present at nearly as many conferences, or publish in journals.

I would like to thank everyone in my research group for their support starting when I was an undergrad. I was able to learn a lot for them, and get involved with many projects due to their generosity, support, and willingness to work with me.

Lastly, I'd like to thank my family for everything they've done to give me this great opportunity.

TABLE OF CONTENTS

Page

LIST OF TABLES

LIST OF FIGURES

Figure Page

SYMBOLS

γ	mean free path
m	mass
v	velocity
T	temperature
Kn	Knudsen number
k_T	thermal diffusion factor
F	Force
p	pressure
A	area
μ	viscosity
f	distribution function
$\mathcal{Q}$	collision integral
d	diameter
α	scattering parameter
ω	viscosity coefficient
σ_T	collision cross section
c_r	thermal velocity
k	thermal conductivity
λ	ratio of specific heats
G	gap
D	self-diffusion coefficient
q	heat flux
Nu	Nusselt number

ABBREVIATIONS

MIKRA	Microscale In-Plane Knudsen Radiometric Actuator
MEMS	Micro-Electro-Mechanical systems
DSMC	Direct Simulation Monte Carlo
DGFS	Discontinuous Galerkin Fast Spectral Method
ESBGK	Ellipsoidal Statistical Bhatnagar-Gross-Krook Method
HS	Hard Sphere
VHS	Variable Hard Sphere
VSS	Variable Soft Sphere
NTC	No-Time Counter

ABSTRACT

Pikus. Aaron M.S., Purdue University, May 2019. Numerical Simulations and Characterization of Thermally Driven Flows on the Microscale. Major Professor: Alina A. Alexeenko.

Large thermal gradients can cause very nonintuitive effects in the flowfield, as flow motion and even a force (often referred to as a Knudsen thermal force) can be induced even with a freestream velocity of zero. These flows can be exploited on the microscale, where temperature gradients of $1\text{K}/\mu\text{m}$ are achievable. These flows have been studied experimentally many times, and it has been shown that Knudsen forces have a bimodal relationship with pressure, where the peak is in the transitional flow regime. It has also been shown that these thermal gradients cause thermal diffusion, or species separation in a mixture.

A MEMS based device called the Microscale In-Plane Knudsen Radiometric Actuator (MIKRA) was developed to use Knudsen forces to calculate pressure and gas composition. The direct simulation Monte Carlo (DSMC) method was used to analyze the device to calculate the device forces and calculate the flowfield. DSMC proved to be a reliable method of simulating these types of flows, as the force results agreed well with experiments, and the DSMC results matched the results of other numerical methods.

N_2 and H_2O mixtures were also simulated, and it was shown that the force is sensitive to the composition. At the same pressure, the force is larger for mixtures dominated by N_2. Heat flux is also larger for N_2 dominated flows.

1. INTRODUCTION

1.1 Motivation

Thermostress convection makes up a very unique and nonintuitive area of gas dynamics, where gas motion is induced by a temperature gradient alone. This gas motion also induces a force, often referred to as Knudsen thermal forces. To generate significant fluid motion and force this way, the thermal gradient must be comparable to the mean free path (λ): $T/(dT/dx) \approx \lambda$.

These flows were experimentally investigated early on with the Crooke's radiometer (1873) [1] and with Knudsen's gauge [2]. Crooke's radiometer consisted of a long thin and narrow platinum vane with black and bright sides exposed to a rarefied environment (Fig. 1.1). External light heats the black side, causing a temperature gradient through the vane. Knudsen's device (Figure 1.2) used evacuated glass bulbs separated by a long narrow tube. He discovered that heating one of the bulbs leads to a high pressure at the hot end and low pressure at the cold end. The momentum imbalance of particles reflecting from these two opposite surfaces produces a net force in both devices.

Exploiting Knudsen forces wasn't practical for a long time since they only become significant under extreme temperature gradients: $\sim$1 K/μm. It is virtually impossible to reproduce such gradients in typical macroscale devices, but it can easily be achieved in the microscale using Micro-Electro-Mechanical systems (MEMS). Given their size, there are numerous emerging MEMS technologies that operate in rarefied conditions, i.e., $Kn \geq 0.1$. Examples of problems where rarefied phenomena cannot be neglected include vacuum-based manufacturing processes and satellites.

MEMS based technologies offer unique opportunities to exploit thermostress convection mechanisms. Passian et. al. [3] used this phenomenon to demonstrate mi-

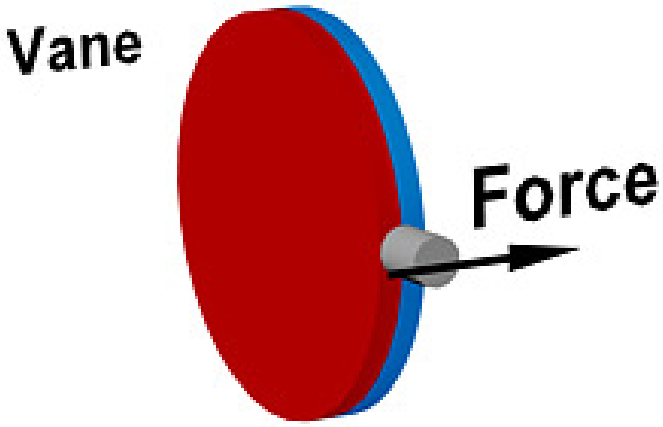

Fig. 1.1.: Crookes Radiometer concept [1]

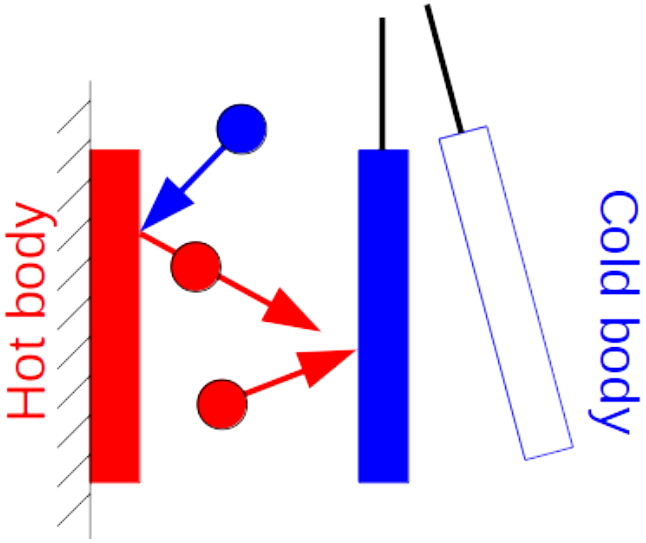

Fig. 1.2.: Concept of Knudsen Gauge [2]

crostructure actuation. He suspended a heated microcantilever over a substrate. Knudsen forces in the gap between the cantilever and substrate led the cantilever tip being deflected. Assuming a constant temperature gradient, this deflection is related to the Knudsen force for gas pressures.

In multi-species flows, however, thermo-stress convection affects the concentration of each species as well. Chapman [4] theorized about the diffusion process of a two species mixture and found that the difference in the concentrations is related to $k_T \nabla \ln T$, where k_T is thermal diffusion factor, and T is the temperature. In most conditions, this coefficient is very low, as a very large temperature gradient is required to make the gradient of $\ln T$ substantial. Therefore, thermal diffusion is rarely considered in practice. In microscale flows, however, the temperature gradient can easily exceed $10^6 K/m$, as previously mentioned. Under such conditions, $k_T \nabla \ln T$ can be signficant.

A lot of work has been done to study these flows. Previous work also includes modeling of these types of flows, not just experiments. Loyalka [5] calculated the Knudsen forces on a hanging wire of a vacuum micro-balance using a linearized Boltzmann equation with Helium as the working gas. They noted a maximum Knudsen force in the transitional regime. Fierro [6] used the Bhatnagar-Gross-Krook (BGK) model for multiple molecular species (Helium, Krypton, Hydrogen, Oxygen) at a range of Knudsen numbers. They noted an inverted parabolic profile of force with respect to the Knudsen number. Alexeenko [7] used the direct simulation Monte Carlo method (DSMC) and the deterministic kinetic ellipsoidal statistical Bhatnagar-Gross-Krook (ESBGK) model to simulate flow around heated micro-beams, and compared those results to results from Navier-Stokes. They estimated the gas-damping coefficients on a moving micro-beam for quasi-static isothermal conditions with all three numerical methods for a range of Knudsen numbers from 0.1 to 1.0. Navier-stokes overestimated the damping force from the gas for Knudsen numbers larger than 0.1, while the ESBGK and DSMC methods produced similar results. They also concluded that the Knudsen force peaks in the transitional regime. Many since have used the various numerical methods to analyze such flows, and concluded that the they can reproduce experimental results [8–10].

1.2 Research Goals

A device concept was previously proposed as a pressure and gas composition sensor (Sec. 3). It is a MEMS based device that exploits thermal convection. Throughout this work, we used numerical methods to study the flow within the device by measuring the forces within the device and heatflux between the gas and solid bodies. By comparing the forces to the experimental results, we intend to show that numerical methods can be used to study these types of flows. Then we study geometrical variations of this type of device, and characterize the device's performance with mixtures.

1.3 Thesis Structure

The remainder of this thesis is structured as follows. The theory behind Knudsen forces is explained in chapter 2, and the mechanisms behind the force near the free molecular and continuum limits are identified. The device of interest through this work is introduced in chapter 3. The concept of operations and experimental results are also included in there. The numerical modeling techniques are discussed in chapter 4, including the theory and the methods used throughout this work. The numerical results are shown in chapter 5, and are compared to experimental results and each other for validation purposes. A new device of similar concept is proposed in chapter 6, the numerical conditions are provided in chapter 8, and the results are provided in chapter 9.

2. THEORY OF KNUDSEN FORCES

A version of this has been published in Vacuum 161 (2019): 130-137 [11].

Knudsen thermal forces are bimodal in nature and achieve their maximum value in the transitional regime where the flow admits neither a free molecular ($Kn \to \infty$) nor a continuum ($Kn \to 0$) behavior [12]. The exact Knudsen number where the force peak occurs can vary significantly based on geometry.

2.1 Free Molecular Limit

Consider a solid body with a hot side and cold side. If the mean free path is a lot larger than the thickness of the body, the flow is in the free molecular regime. In the free molecular limit, collisions between molecules can be neglected and the Knudsen force are solely a result of ballistic interactions of gas molecules on the body surface (Figure 2.1). The temperature difference means molecules reflected from the hot side exchange a higher amount of momentum than those reflected from the cold side. The expression for the Knudsen force generated by a simple gas on a flat vane with opposite cold and hot sides is given by [2]

$$F = \frac{p_\infty A}{2}\left(-1 + \sqrt{\frac{T_H}{T_C}}\right), \tag{2.1}$$

where p_∞ is the ambient pressure, A is the exposed area of the body, and T_H and T_C are the temperatures of hot and cold sides, respectively. This result assumes a diffuse gas-surface interaction, meaning the momentum and internal energy states of molecules thermally equilibriate to the wall conditions during collisions.

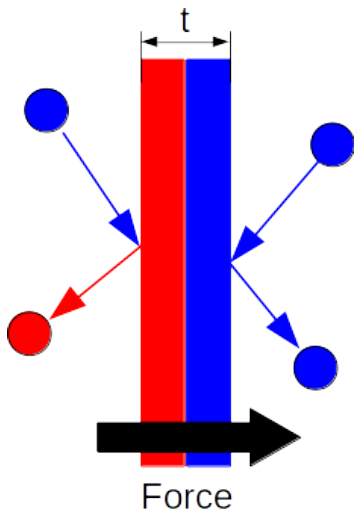

Fig. 2.1.: Simple vane with a hot left side and cold right side. In free molecular flows, the Knudsen force is caused by ballistic interactions of gas molecules on both sides of the surface.

2.2 Continuum Limit

As the mean free path around the body becomes smaller than the body thickness, the flow approaches the continuum limit. Although the ballistic interactions still take place as in the free molecular case, those become negligible. The Knudsen thermal force is dominated by thermal stresses within the gas, which can be called the edge effect (Figure 2.1). This means cold molecules heat up as they approach the edge of the hot side, causing a force from hot to cold concentrated at the vane tips. The force is inversely proportional to pressure as the flow approaches the continuum limit.

This behavior can be discussed using a perturbation analysis of the distribution function of molecular velocity f with Chapman-Enskog theory [4]. According to Kogan et al. [13], the stress tensor P_{ij} for high-order expansions can be written as

$$P_{ij} = p\delta_{ij} + \tau_{ij}^{(1)} + \tau_{ij}^{(2)} + ... \tag{2.2}$$

where

$$\tau_{ij}^{(1)} = -2\mu\frac{\partial u_i}{\partial x_j}, \tag{2.3}$$

$$\tau_{ij}^{(2)} = K_1 \frac{\mu^2}{p} \frac{\partial u_k}{\partial x_k} \frac{\partial u_i}{\partial x_j} + K_2 \frac{\mu^2}{\rho T} \frac{\partial^2 T}{\partial x_i x_j} + K_3 \frac{\mu^2}{\rho T^2} \frac{\partial T}{\partial x_i} \frac{\partial T}{\partial x_j}. \tag{2.4}$$

The first term in Eq. (2.2) represents the zeroth-order (equilibrium) solution, or the Euler equations. By summing the first two terms, we get the Navier-Stokes equations for near-equilibrium conditions. Second-order expansion gives us Burnett equations, where $\tau_{ij}^{(2)}$ is a function thermal gradients in addition to velocity. The respective viscosity μ and $K(\sim 1)$ coefficients depend on the gas species. The terms depending on thermal gradients scale with Kn^2 [14]. In sufficiently low speed and highly nonisothermal flows, these terms can induce significant convective transport.

Thermostress convection exists in all flows with nonuniform temperature profiles. There are three elementary thermally driven flow mechanisms, as suggested by Sone [15]: thermal creep due to temperature gradient parallel to the body surface [16], thermal stress slip flow due to gas phase temperature gradients normal to the body surface [17]; and nonlinear thermal stress flow due to large $\frac{\partial^2 T}{\partial x_i \partial x_j}$ and $\frac{\partial T}{\partial x_i} \frac{\partial T}{\partial x_j}$ terms [13]. The combination of these three mechanisms is referred to as thermal edge flow, and which takes plane in rarefied flows around surfaces with small curvatures. These mechanisms are further described in [15, 18, 19].

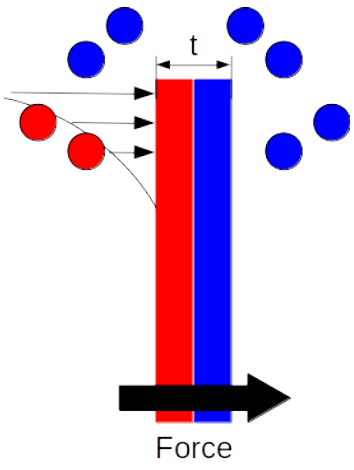

Fig. 2.2.: Simple vane with a hot left side and cold right side. In continuous flows, the Knudsen force is caused by the edge effect.

3. MIKRA DEVICE

A version of this chapter, including the figures, has been published in Journal of Microelectromechanical Systems 26.3 (2017): 528-538 [20].

More complicated device concepts have been proposed to create a practical application for Knudsen thermal forces. By stacking multiple heaters, one can enhance the force [20–22]. This concept served as the inspiration for the device concept studied throughout this work.

The Microscale In-Plane Knudsen Radiometric Actuator (MIKRA) [20] is a device developed at Purdue (Figure 3.1), and consists of multiple hot and cold beams, which are all on the microscale. It relies on in-plane motion of a shuttle mass actuated by Knudsen thermal forces. The shuttle is suspended 4 μm above the substrate. It consists of a central support member with 12 extended beams (which are the cold beams). Fixed heater beams (or hot beams) are located 20 μm away from the shuttle beams. When electrical current is applied, the temperature of the heater beams increases, causing a temperature gradient on the order of 10^6 K/m. The shuttle actuates away from the heater beams. This deflection is measured by comb capacitors at the edge of the device. More information about the manufacturing and operations of the device can be found in [20].

3.1 Knudsen Force Measurements

Experimentally measured Knudsen forces on the shuttle are shown in Figure 3.2 with air and helium as the working fluids at three different heating element powers of 75, 100, and 125 mW. Also provided are the experimental results of Passian et al [3] for a cantilever suspended over an underlying substrate.

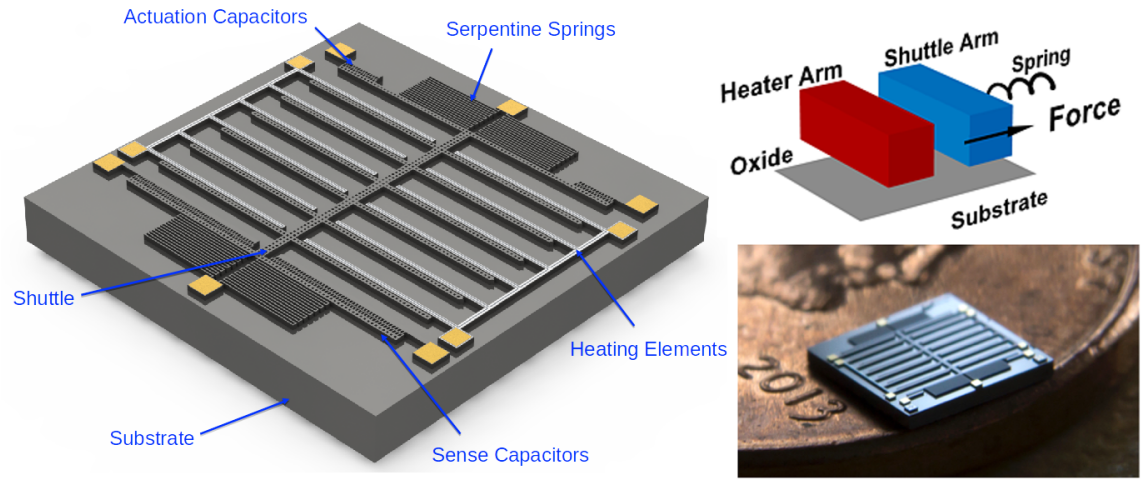

Fig. 3.1.: CAD representation and SEM images of the MIKRA device.

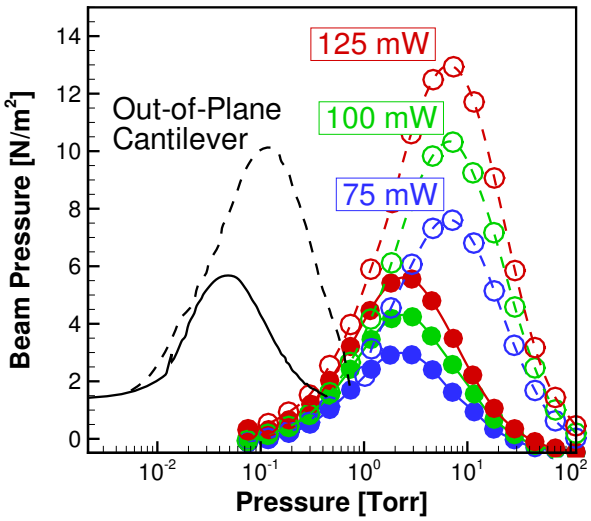

Fig. 3.2.: Experimentally measured force in air (solid) and helium (dashed) for heating element power levels of 75, 100, and 125 mW. Results of Passian et al. are also provided [3]

The bell-shaped force profile as a function of pressure is characteristic of thermostress convection. This distribution stems from the bimodal nature of the Knudsen force, a result which is expected from equations (2.1) and (2.2). In the free molecular

limit, the force output is proportional with pressure as a result of the ballistic interaction between the molecules and the shuttle surface. Molecules striking the shuttle from within the gap have more kinetic energy than those on the opposing face, leading to a net repulsive force between the bodies. In the continuum limit, the force results from the non-equilibrium conditions in the gap separating shuttle and heated arms. In this case, fluid is actuated towards the centerline of the shuttle arm from the edges. The impinging streams from the upper and lower surfaces roll up into a pair of vortices which generate a high pressure circulation zone in the gap. This can be seen clearly in the flowfields presented in section 5.

Fig 3.2 reveals an attraction between the beams, or a negative force, in the free molecular and near continuum regimes. In the free molecular regime the Knudsen number within the gap is large, producing Knudsen forces which are small. The Knudsen number between the shuttle arm and the heater arm of the adjacent pair is within the transitional regime, which might lead to a negative net force. In the continuum regime, the negative force is believed to derive from buoyancy effects. The heated fluid within the gap has lower density that that of the surroundings and thus rises. The induced motion leads to a reduced static pressure, acting to pull the heater and shuttle arms together.

Figure 3.2 shows that the Knudsen thermal force with Helium as the working fluid is consistently larger than in air. This behavior is a result of differences in molecular thermal speed between species. The mean free path of helium is larger than that of air. Thus, a higher ambient pressure is required to achieve an identical Knudsen number. The large collision frequency at elevated pressures ultimately leads to the enhanced force output exhibited by helium.

4. NUMERICAL MODELING

Several subsections within this chapter, including the figures, has been published in Journal of Microelectromechanical Systems 26.3 (2017): 528-538 [20]. A few subsections will also be submitted to Physics of Fluids [23].

Numerical modeling was also done to assist with the design of the MIKRA as well as to understand the flowfields within this sensor for better interpretations of the experimental results and for other potential applications. The spatial resolution needed for flowfield visualization within this sensor makes this task not feasible experimentally.

4.1 Boltzmann Equation

The flow within this sensor falls into the rarefied gas regime, which is observable in low pressure environments and on the microscale. This is dictated by the Knudsen number, which is equal to the mean free path divided by the characteristic length of the flow (λ/L). The mean free path varies with pressure. For the cases simulated in this work, it varied from about 6 microns to 230 microns. The characteristic length of the flow was chosen as the distance between the shuttle and heater arms, which is 20 μm, meaning the Knudsen number varied from about 0.3 to 11.5.

Such high Knudsen number conditions along with the temperature gradients within the flow cause the Navier-Stokes equations to break down. This means a kinetic-based solution is necessary, as it can properly account for the rarefied gas effects as well as the temperature gradients.

To correctly simulate this flow, we must solve the full Boltzmann equation, which describes the evolution of the space and velocity distribution functions in six dimen-

sional space. This allows us to model dilute gasses at the molecular level for a wide range of Knudsen numbers.

Consider a mixture of gases with at least two different species. Each species is represented by a distribution function $f_{(i)}(t, x, v)$, where t is the time, x is the particle's position, and v is the particle's velocity. Thus, $f_{(i)}(t, x, v)$ tells us the number of particles of species i that can be found in an infinitesimally small space $dxdv$ centered at the point (x, v). The time evolution of the distribution function $f_{(i)}$ is described by the multi-species Boltzmann equation written as [24, 25]

$$\partial_t f_{(i)} + v\nabla_x f_{(i)} = \sum_{j=1}^{s} \mathcal{Q}^{ij}(f_{(i)}, f_{(j)}), \quad i = 1, \ldots, s. \tag{4.1}$$

where s is the number of different species, and $\mathcal{Q}^{ij}$ is the collision term that models binary collisions between species i and j, and its only valid in the velocity space:

$$\mathcal{Q}^{(ij)}(f_{(i)}, f_{(j)})(v) = \int_{\mathbb{R}^3}\int_{S^2} \mathcal{B}_{ij}(v - v_*, \sigma) \times [f^{(i)}(v')f^{(j)}(v'_*) - f^{(i)}(v)f^{(j)}(v_*)]d\sigma dv_*, \tag{4.2}$$

where (v, v_*) and (v', v'_*) denote the pre- and post- collision velocity pairs. During collisions, momentum and energy are conserved:

$$\begin{aligned} m_i v + m_j v_* &= m_i v' + m_j v'_*, \\ m_i|v|^2 + m_j|v_*|^2 &= m_i|v'|^2 + m_j|v'_*|^2, \end{aligned} \tag{4.3}$$

where m_i, m_j represent the mass of particles of species i and j respectively. One can parameterize v' and v'_*:

$$\begin{aligned} v' &= \frac{v + v_*}{2} + \frac{(m_i - m_j)}{2(m_i + m_j)}(v - v_*) + \frac{m_j}{(m_i + m_j)}|v - v_*|\sigma, \\ v'_* &= \frac{v + v_*}{2} + \frac{(m_i - m_j)}{2(m_i + m_j)}(v - v_*) - \frac{m_i}{(m_i + m_j)}|v - v_*|\sigma, \end{aligned} \tag{4.4}$$

with σ being a vector varying on the unit sphere S^2. $\mathcal{B}_{ij}$ is the collision model characterizing the interaction potential between particles. It can be shown that

$$\begin{aligned} \mathcal{B}_{ij} &= B_{ij}(|v - v_*|, \cos\chi), \\ \cos\chi &= \frac{\sigma \cdot (v - v_*)}{|v - v_*|}, \end{aligned} \tag{4.5}$$

where χ is the deflection angle between $v - v_*$ and $v' - v'_*$.

Given the interaction potential between particles, B_{ij} can be calculated using the classical scattering theory:

$$B_{ij}(|v - v_*|, \cos\chi) = |v - v_*|, \\ \Sigma_{ij}(|v - v_*|, \chi) \tag{4.6}$$

where Σ_{ij} is the differential cross-section given by

$$\Sigma_{ij}(|v - v_*|, \chi) = \frac{b_{ij}}{\sin\chi} \left| \frac{db_{ij}}{d\chi} \right|, \tag{4.7}$$

with b_{ij} being the impact parameter.

The explicit form of Σ_{ij} is often hard to obtain since b_{ij} is related to χ. However, the interaction potential chosen is very important to the accuracy of the simulation along with the computational complexity. VSS makes a key simplification by assuming:

$$\chi = 2\cos^{-1}\{(b_{ij}/d_{ij})^{1/\alpha_{ij}}\}, \tag{4.8}$$

where α_{ij} is the scattering parameter, and d_{ij} is the diameter calculated for the VHS model [26]:

$$d_{ij} = d_{\mathrm{ref},ij} \left[\left(\frac{2k_B T_{\mathrm{ref},ij}}{\mu_{ij}|v - v_*|^2} \right)^{\omega_{ij}-0.5} \frac{1}{\Gamma(2.5 - \omega_{ij})} \right]^{1/2}, \tag{4.9}$$

where Γ is the Gamma function, μ_{ij} is the reduced mass equal to $\frac{m_i m_j}{m_i + m_j}$, $d_{\mathrm{ref},ij}$ is the reference diameter, $T_{\mathrm{ref},ij}$ is the reference temperature, and ω_{ij} is the viscosity index. Substituting the eqns. (4.7)-(4.9) into (4.6), B_{ij} can be calculated:

$$B_{ij} = b_{\omega_{ij},\,\alpha_{ij}} \, |v - v_*|^{2(1-\omega_{ij})} \, (1 + \cos\chi)^{\alpha_{ij}-1}, \tag{4.10}$$

where $b_{\omega_{ij},\alpha_{ij}}$ is a constant given by

$$b_{\omega_{ij},\,\alpha_{ij}} = \frac{d^2_{\mathrm{ref},ij}}{4} \left(\frac{2k_B T_{\mathrm{ref},ij}}{\mu_{ij}} \right)^{\omega_{ij}-0.5} \frac{\alpha_{ij}}{\Gamma(2.5 - \omega_{ij})\, 2^{\alpha_{ij}-1}}. \tag{4.11}$$

In VSS, α_{ij} is between one and two. ω_{ij} is between 0.5 and 1.0. To go from VSS to VHS, we set α_{ij} to 1. The collision model can be further simplified, where by setting

ω_{ij} to equal 0.5, the model is simplified to HS. If ω_{ij} is set to 1.0, we have Maxwellian molecules.

Given the distribution function $f_{(i)}$, the number density, mass density, velocity, and temperature of species i are defined as

$$\begin{aligned} n_{(i)} = \int_{\mathbb{R}^3} f_{(i)} dv, \quad \rho_{(i)} = m_{(i)} n_{(i)}, \\ u_{(i)} = \frac{1}{n_{(i)}} \int_{\mathbb{R}^3} v f_{(i)}\, dv, \\ T_{(i)} = \frac{m_{(i)}}{3 n_{(i)} k_B} \int_{\mathbb{R}^3} (v - u_{(i)})^2 f_{(i)}\, dv. \end{aligned} \tag{4.12}$$

The total number density, mass density, and velocity are given by

$$n = \sum_{i=1}^{s} n_{(i)}, \quad \rho = \sum_{i=1}^{s} \rho_{(i)}, \quad u = \frac{1}{\rho} \sum_{i=1}^{s} \rho_{(i)} u_{(i)}. \tag{4.13}$$

Further, the diffusion velocity, stress tensor, and heat flux vector of species i are defined as

$$\begin{aligned} v_{(i)}^D = \frac{1}{n_{(i)}} \int_{\mathbb{R}^3} c f_{(i)}\, dv = u_{(i)} - u, \\ \mathbb{P}_{(i)} = \int_{\mathbb{R}^3} m_{(i)} c \otimes c f_{(i)}\, dv, \\ q_{(i)} = \int_{\mathbb{R}^3} \frac{1}{2} m_{(i)} c |c|^2 f_{(i)}\, dv, \end{aligned} \tag{4.14}$$

where c is the peculiar velocity. Finally, the total stress, heat flux, pressure, and temperature are given by

$$\mathbb{P} = \sum_{i=1}^{s} \mathbb{P}_{(i)}, \quad q = \sum_{i=1}^{s} q_{(i)}, \quad p = n k_B T = \frac{1}{3} \mathrm{tr}(\mathbb{P}). \tag{4.15}$$

4.2 Direct Simulation Monte Carlo Method

The Direct Simulation Monte Carlo (DSMC) method [26] is a stochastic method that solves the Boltzmann Equation, and is often applied to rarefied and non-equilibrium flows. DSMC can simulate flows of any Knudsen number by using computational particles to simulate the behavior of the real gas, where each computational particle

represents a large number of real particles. Each computational particle has it's own position, velocity, and internal energies.

To initialize the DSMC simulation, the simulation domain is discretized into grid cells. Each cell is populated with representative particles, and the initial position, velocity, and properties of each particle is set. Then, for each timestep, the particles are moved, the collisions are calculated, and the properties of each grid cell and surface element are sampled.

During the movement phase, each particle is moved according to its velocity. This motion is collisionless, meaning the velocity doesn't change here. Then the collision phase takes place, which is the only mechanism with which velocity can change.

The collision scheme used in the collision phase is very important, as the correct collision frequency must be reproduced, or else the simulation will be very inaccurate. One very common collision scheme is the no time counter (NTC) scheme [26]. In NTC, the number of expected collisions within each cell (N_{coll}) is computed (Eq. 4.16), then two particles are randomly selected within their cell. Their collision is accepted with a probability equal to $\sigma_T c_r/(\sigma_T c_r)_{max}$, where σ_T is the total collision cross section for the collision pair, and c_r is the relative speed of the collision pair. Two particles are randomly selected to collide recursively until it is done N_{coll} times.

$$N_{coll} = \frac{N(N-1)F_{num}(\sigma_T c_r)_{max}\Delta t}{2\Delta V} \tag{4.16}$$

where N is the number of computational particles in the cell, F_{num} is the ratio of real to computational particles, σ_T is the total collision cross section for the collision pair, and c_r is the relative speed of the collision pair, Δt is the simulation timestep, and V is the cell volume.

Note that $\sigma_T c_r$ is the effective volume swept by the collision pair. $(\sigma_T c_r)_{max}$ is the maximum volume swept. By taking the ratio, DSMC normalizes the probability of the collision occurring which speeds up the DSMC simulation. The maximum volume is selected at the beginning of the simulation for each cell, and is updated should a collision pair have a larger swept volume.

Each collision is described by the interaction potential. The specific interaction potential chosen has a substantial effect on the simulation accuracy and computational complexity. Initially, the only collision model used in DSMC was the hard sphere (HS) interaction model [27], which is a purely repulsive interaction model. The HS model deviates from experimental data even for common gases [28] due to the square-root viscosity variation with temperature. Variable hard sphere (VHS) was proposed [26] to correctly and efficiently model viscosity, and it's commonly used for single species DSMC simulations. However, VHS doesn't reproduce diffusive transport correctly, which is a factor in multi-species flows [29, 30]. Several models were proposed to correct this issue, including variable soft sphere (VSS) [30], which is also a repulsive interaction. VSS adds a scattering coefficient α that allows DSMC to correctly reproduce diffusion along with viscosity.

One other key feature in the collision process worth discussing is the post-collisional internal energies of each molecule. The Larsen-Borgnakke model [31] is a phenomenological model that is very common in DSMC. It samples the post collisional internal energies of the molecules from the equilibrium distribution function associated with the notional temperature which is based on the total energy of the collision. This approach allows for DSMC to reproduce realistic behavior of the gas while being computationally efficient.

Finally, the sample phase consists of sampling over all cells to calculate macroscopic properties. The properties from each simulated molecule, including their velocities and internal energies, are averaged in each cell to compute the macroscopic properties, or bulk properties, such as density, bulk velocity, temperature, and pressure.

The DSMC solver SPARTA [32] developed by Sandia Labs was used in this work. The molecular collisions are described by the No-Time Counter (NTC), Variable Hard Sphere (VHS), and Larsen-Borgnakke (LB) models.

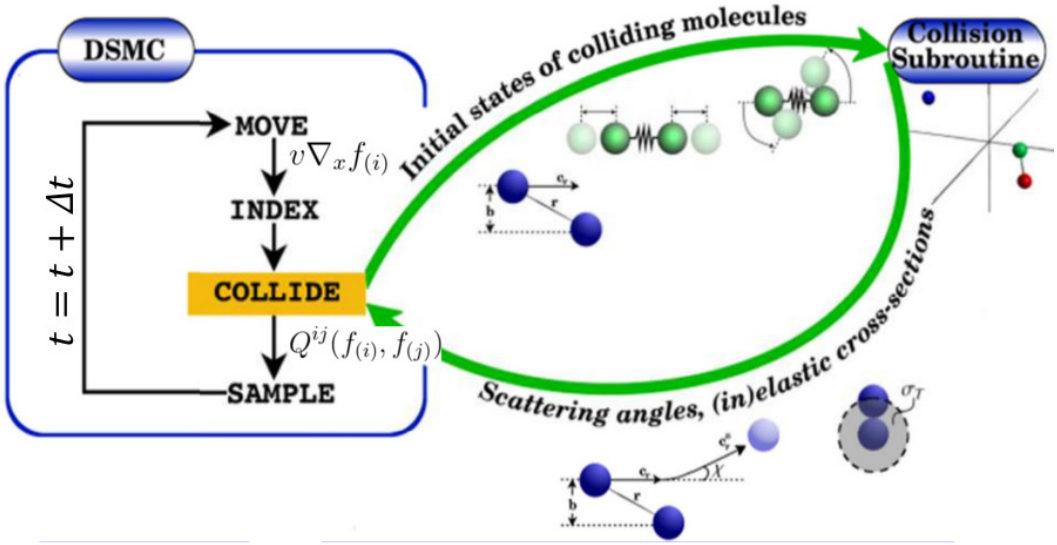

Fig. 4.1.: DSMC process [26]

4.3 Flow and Numerical Parameters

In order to setup the simulation, the DSMC parameters, problem dimension, domain size, mesh, number of computational particles per cell, and timestep had to be set to best represent the problem. The DSMC parameters chosen were just the standard ones for the VHS collision model for N_2, shown in Table 4.1.

The length of the heater and shuttle arms is much larger than the gap between them. Also, it was assumed that there was limited interaction between each heater-shuttle arm pair. Therefore, the 2D domain and boundary conditions shown in Fig. 4.2 can be used to simulate the MIKRA flowfields. In this figure, T_S, T_H, and T_C represent the temperatures of the shuttle, heater arm, and cold arm, respectively. T_∞ and P_∞ correspond to the freestream temperature and pressure, respectively.

The number of simulated particles was around 4.5 million, which corresponds to about 100 computational particles per cell. The timestep was one nanosecond. There were 300 by 150 collision cells in the x and y directions, respectively. Lastly, the entire simulation involved 5.1 million timesteps, where the first 100,000 timesteps

Table 4.1.: VHS model parameters and number of rotational degrees of freedom (DOFs) [26]

Reference temperature, T_{ref} (K)	273
Reference diameter, d_{ref} (Å)	4.17
Viscosity index, ω (-)	0.74
Scattering parameter, α (-)	1.00
Rotational #DOFs, ζ_R (-)	2

were treated as unsteady and just used to initialize the simulation, meaning they were not included in the sampling of the flowfield or force values.

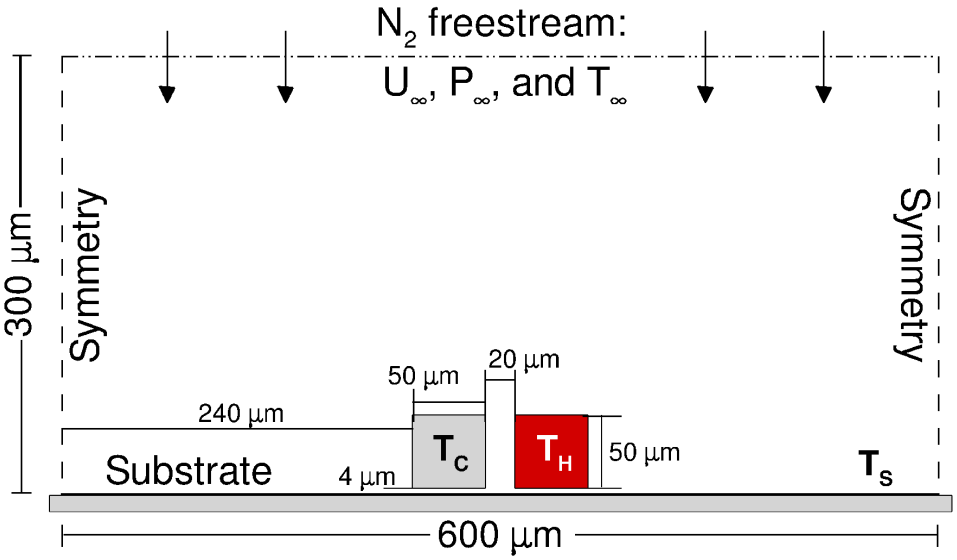

Fig. 4.2.: The boundary conditions used for the DSMC simulations were chosen based on the experimental setup. The domain size allowed for accurate flowfield visualization.

Note that the device heater temperatures were very nonuniform, and the temperature between the 12 different heater beams varied. Therefore, two sets of T_H and T_C values were considered at each pressure. By setting the upper and lower temperature bounds, we can set the upper and lower bounds for the numerical forces which should envelope the experimental forces. The simulated conditions are listed in table 4.2.

Table 4.2.: Pressure, Knudsen number, and temperature used in DSMC simulations corresponding to experiments at 100 mW heater power

		Arm 1		Arm 3	
P (Torr)	Kn (-)	T_C (K)	T_H (K)	T_C (K)	T_H (K)
0.188	11.49	302	330	306	370
0.465	4.64	303	326	306	370
1.163	1.85	303	329	306	363
2.903	0.74	302	327	306	356
7.246	0.30	300	315	304	331

The pressure and shear along the surfaces of the shuttle arm were computed within DSMC and used to calculate the forces. The shear force was about two orders of magnitude less than the pressure forces, meaning the shear forces were negligible. The simulations were validated by comparing the calculated forces to the those measured during the experiments.

In order to better map the surface properties, they were measured with a higher spatial resolution. Each side of the shuttle arm was divided into 20 panels, and the pressure and shear forces were measured along each panel. This gave a distribution of the pressure force over each side.

Flowfields were also of interest throughout this work. The temperature and speed flowfields were plotted, and streamlines were added to the speed flowfield.

4.4 Verification

A verification study was done to make sure the DSMC parameters chosen produced accurate results. DSMC simulations become more computationally expensive as pressures increase because of the reduced mean free path and mean collision times. Therefore the most challenging case throughout this work was the highest pressure case, which was at 7.246 Torr (966 Pa), and the verification study was done for this case. The verification cases included testing less computational particles per cell (20), more computational particles per cell (200), a finer mesh (twice as fine in each dimension), timestep that is one fifth of the standard case, and a timestep that is five times larger. Lastly, there was also a case that was ran for a longer period of time in order to ensure that steady state was reached. The verification cases showed some variation, but these variations were well within the experiment's margin of error.

Table 4.3.: Verification Cases

Case	Test Name	Timesteps	Force (μN)
1	Standard	5.1e6	1.232
2	Less Particles/cell	5.1e6	1.263
3	More Particles/cell	2.1e6	1.130
4	Finer Grid	5.1e6	1.216
5	Reduced Timestep	25e6	1.303
6	Increased Timestep	1.0e6	1.292
7	Standard-Extended	10.1e6	1.169

4.5 Discontinuous Galerkin Fast Spectral Method

The flowfields were also compared to two other numerical methods, presented in the Results section. Since DSMC is a statistical method, noise is an issue in low speed flows. The recently developed discontinuous Galerkin fast spectral (DGFS)

method [23, 33] fixes many of these issues that DSMC has, and therefore was used as a flowfield verification method. DGFS allows high order accuracy in physical and velocity space, along with collision models including VHS and VSS. Compared to DSMC, it can simulate low-speed flows with smooth and noise-free solutions, such as those in MIKRA.

DGFS solves the Boltzmann equation directly (4.1), where the transport term is discretized by the classical DG method and the collision term (integral in v) is discretized by the fast Fourier spectral method [23, 34]. The discretized system is then advanced in time using the Runge-Kutta method.

The coupling of two kinds of methods (DG in the physical space and spectral method in the velocity space) is possible due to the special structure of the Boltzmann equation – the collision operator acts only in v wherein t and x can be treated as parameters. Simply speaking, given the distribution functions $f_{(i)}$ and $f_{(j)}$ of species (i) and (j) at N^3 velocity grid, the fast Fourier spectral method produces $\mathcal{Q}_(i,j)(f_{(i)}, f_{(j)})$ at the same grid with $O(MN_\rho N^3 \log N)$ complexity, where $M \ll N^2$ is the number of discretization points on the sphere and $N_\rho \sim O(N)$ is the number of Gauss-Legendre quadrature/discretization points in the radial direction needed for low-rank decomposition. Further details can be found in Refs. [23, 33].

The overall DGFS method is simple from mathematical and implementation perspective; highly accurate in both physical and velocity spaces as well as time; robust, i.e. applicable for general geometry and spatial mesh; exhibits nearly linear parallel scaling; and directly applies to general collision kernels needed for high fidelity modelling. Due to these features, we compare DSMC results to DGFS.

4.6 Ellipsoidal Statistical Bhatnagar-Gross-Krook Method

The ellipsoidal statistical Bhatnagar-Gross-Krook method (ESBGK) [35] makes an approximation for the collision term. For this method, the collision term is represented

by $\mathcal{S}$ for single species, instead of the more common $\mathcal{Q}$. $\mathcal{S}$ needs to meet the following four properties:

1. Conservation of mass, momentum, and energy are met
2. Entropy production is always positive
3. $\mathcal{S}$ has a specific form such that the phase density in equilibrium is a Maxwellian
4. The Prandtl number is about 2/3 for all monoatomic gases

The ESBGK collision operator is simplified to a relaxation type kernel given as:

$$\mathcal{S} = \nu \left(f_\gamma - f \right) \tag{4.17}$$

where f_γ is the local equilibrium function, and ν is collision frequency. For ESBGK, f_γ is anisotropic Gaussian given as

$$f_\gamma^{ESBGK} = \frac{\rho}{m\sqrt{\det(2\pi\lambda_{ij})}} \exp\left(-\frac{1}{2}\lambda_{ij}^{-1} c_i c_j \right) \tag{4.18}$$

$$\lambda_{ij} = RT\delta_{ij} + (1 - \frac{1}{Pr})\frac{p_{ij}}{\rho} \tag{4.19}$$

It can be shown that ESBGK satisfies the four conditions [36]. Note that kinetic models like ESBGK have only been derived for single species. Therefore, DSMC can be compared to ESBGK for validation purposes for single species cases, but not for mixtures.

5. MIKRA RESULTS AND DISCUSSION

A version of this chapter, including the figures, has been published in Journal of Microelectromechanical Systems 26.3 (2017): 528-538 [20].

Figures 5.1 and 5.2 below show the non-intuitive flowfield structure within the sensor. All of the vortices appear in near zero velocities, and are caused only by the thermal gradient between the two beams. The vortices, which contribute to the force (especially for lower pressures) vary with gas composition as well as pressure. This visualization clarifies how this sensor is able to associate the force with the ambient pressure and gas composition. The temperature flowfield around the heater arm is shown in Fig. 5.3. As the flow gets more rarefied, the contours become less smooth. This is expected, as with less particles, those that collide with the heater travel more distance before colliding with other particles, so the stand off distance for the contours is larger in more rarefied environments.

The pressure distribution along the left and right sides of the shuttle arm 5.4 shown below for the Kn = 0.78 case. As expected, the pressure from the right side is greater than the pressure from the left side, meaning the shuttle arm would be pushed away from the heater arm. The pressure is highest at the center. The flowfield shows that the vortices are strongest at the top and bottom of the shuttle arm, and are weakest near the center, which suggests the pressure would be highest at the center, as shown in the pressure distribution.

The forces calculated by DSMC were compared to experimental results to validate the simulations, as shown in Figure 5.5. There are two lines for DSMC results because, as discussed earlier, the temperature of the heater arms varied significantly, and it was decided that there should be ten cases instead of just five.

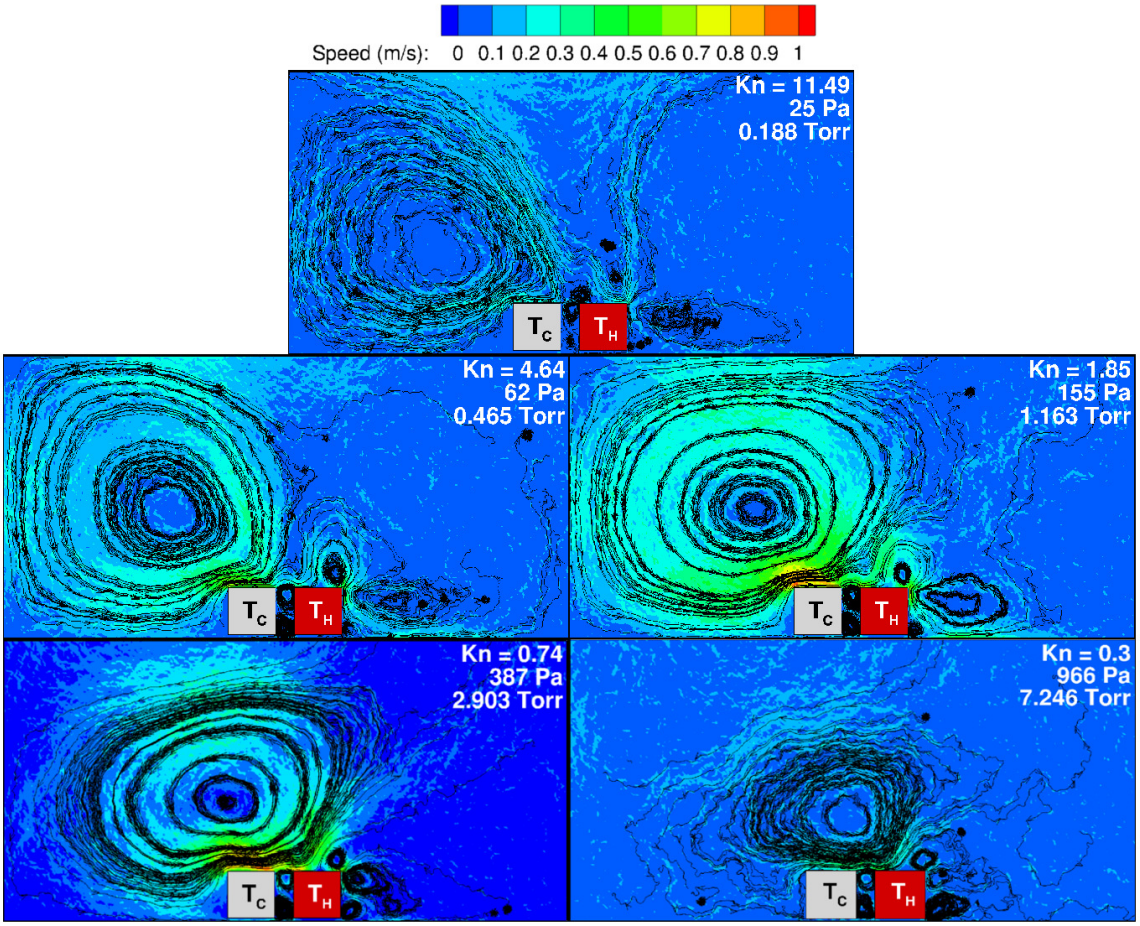

Fig. 5.1.: MIKRA speed and streamline distributions for different freestream and shuttle-heater conditions.

Good agreement is seen between the results, as the bimodal nature of the force and the peak were captured by both DSMC results, which agree to the experiments. The simulation didn't account for a few factors that were present in the experiments, and could have caused some differences between the results. First, the shuttle arm moved slightly during experiments for force measurements, where as the DSMC simulations assumed that the geometry didn't change. The change in the gap would change the Knudsen number. Also, 3D effects, non-uniformities in the temperature along each heater arm, and coupling effects between the heater-shuttle arm pairs could cause

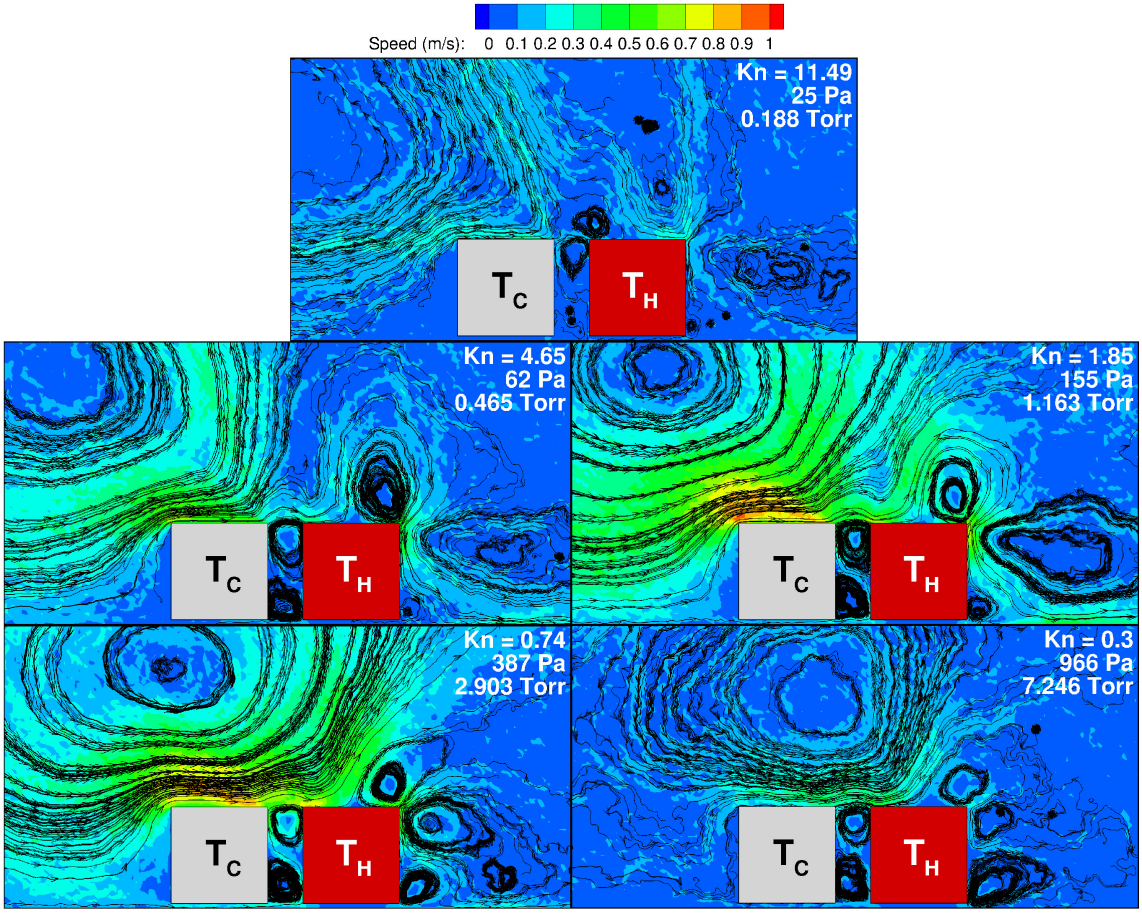

Fig. 5.2.: Amplified view with focus on vortices around the heater arm.

slight differences in the force. Overall, good agreement was observed between the DSMC and experimental results, meaning that that DSMC can be used to study the present application, as well as similar problems with different applications.

The DSMC flowfield results were compared to DGFS. Here, the speed, temperature, and number density flowfields are compared for the Kn=1.85 case. For each of these plots, the DGFS contours (red) have been overlaid on the DSMC contours (black). The temperature and number density flowfields (Figures 5.6,5.7) show very good agreement. Figure 5.8 shows significant statistical fluctuations in DSMC (thin

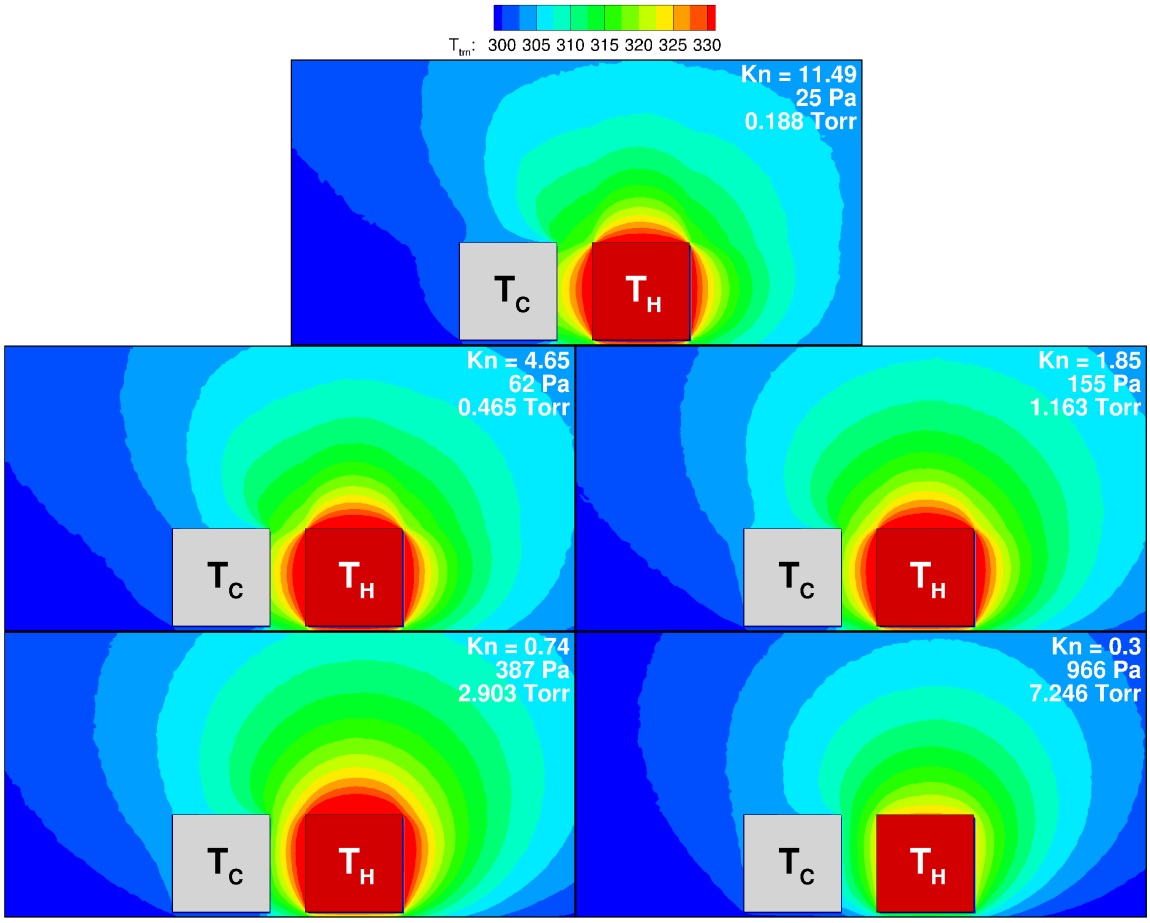

Fig. 5.3.: MIKRA temperature distributions around heater arm.

black lines). The fluctuations are such that without the streamlines and the DGFS contour lines, it's impossible to see the flow structure.

We also compare the variation of flow properties along the vertical centerline ($x = 300\mu m$, $0 \leq y \leq 300\mu m$). We observe a fair agreement between DSMC and DGFS results ignoring the statistical noise. In particular, figures 5.10 and 5.9 show really good agreement. We observe peak temperatures near the edges of hot and cold vanes ($30 \leq y \leq 60\mu m$). The major differences in the in the speed centerline plots can be attributed to noise in the DSMC results.

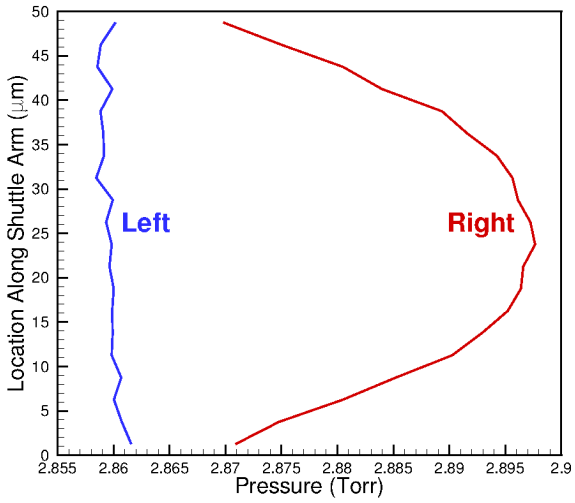

Fig. 5.4.: Pressure distribution along the shuttle arm.

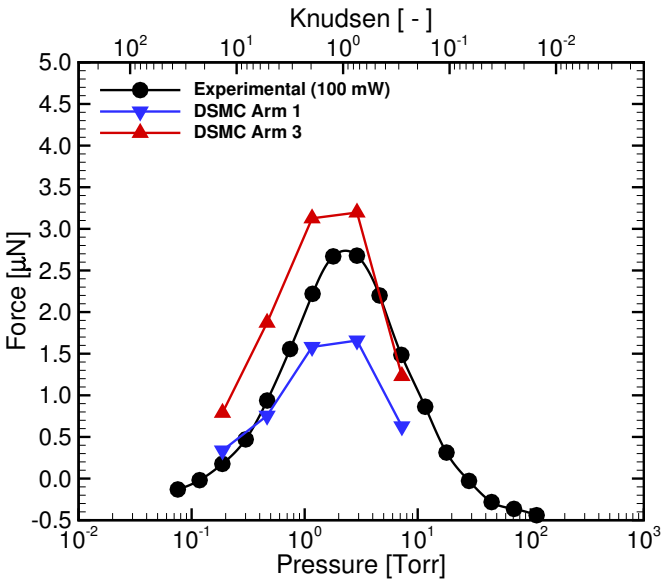

Fig. 5.5.: Force comparison: DSMC vs experimental

Finally, we compare the forces to those of ESBGK. The difference in the forces is 8.1% at the peak, which was considered very good agreement for the purposes of this comparison.

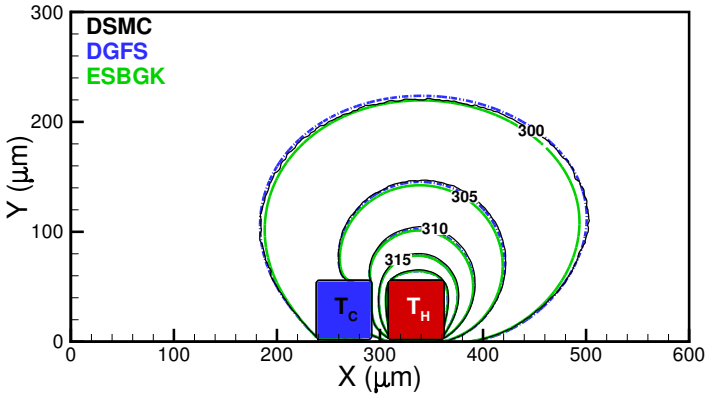

Fig. 5.6.: Temperature flowfield comparison for DSMC, DGFS, and ESBGK

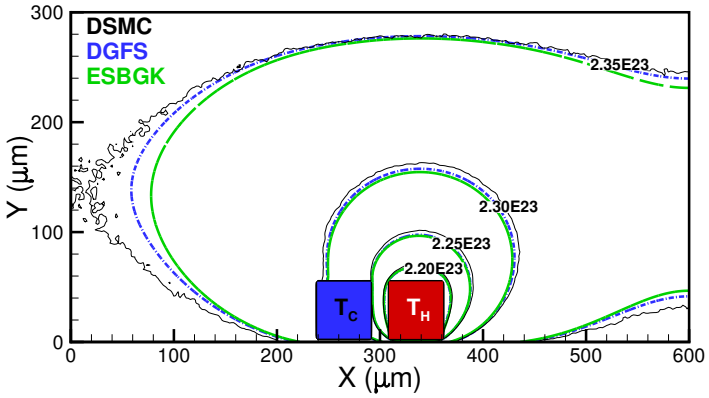

Fig. 5.7.: Number density flowfield comparison for DSMC, DGFS, and ESBGK

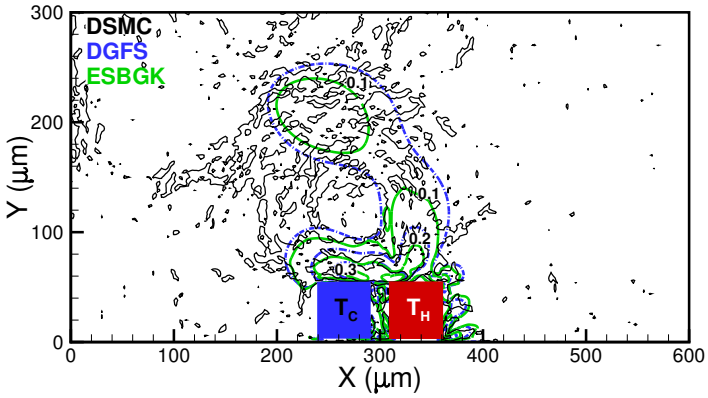

Fig. 5.8.: Speed flowfield comparison for DSMC, DGFS, and ESBGK

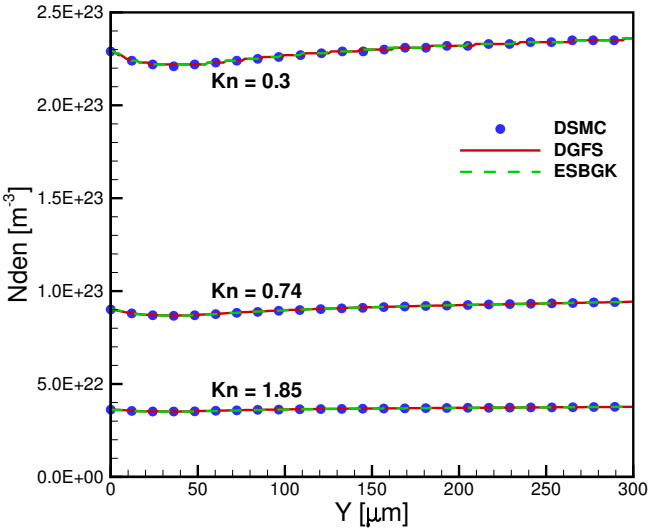

Fig. 5.9.: Number density along centerline comparison for DSMC, DGFS, and ESBGK at multiple Knudsen numbers

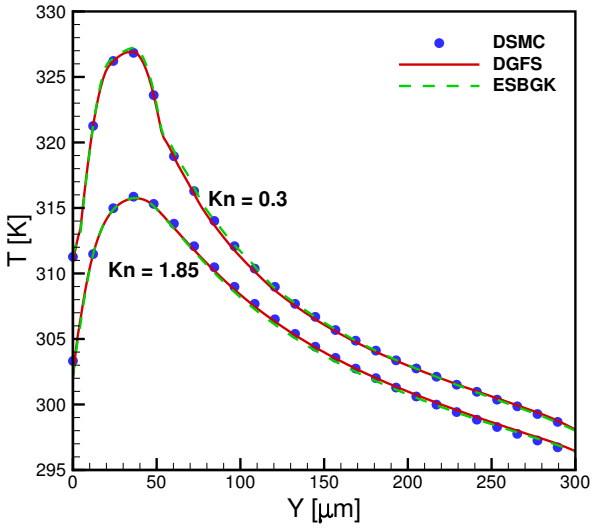

Fig. 5.10.: Temperature along centerline comparison for DSMC, DGFS, and ESBGK at multiple Knudsen numbers

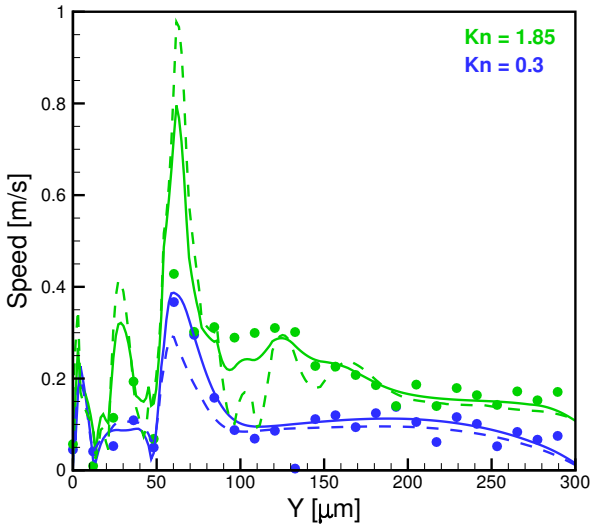

Fig. 5.11.: Speed along centerline comparison for DSMC (circle), DGFS (solid), and ESBGK (dashed) at multiple Knudsen numbers

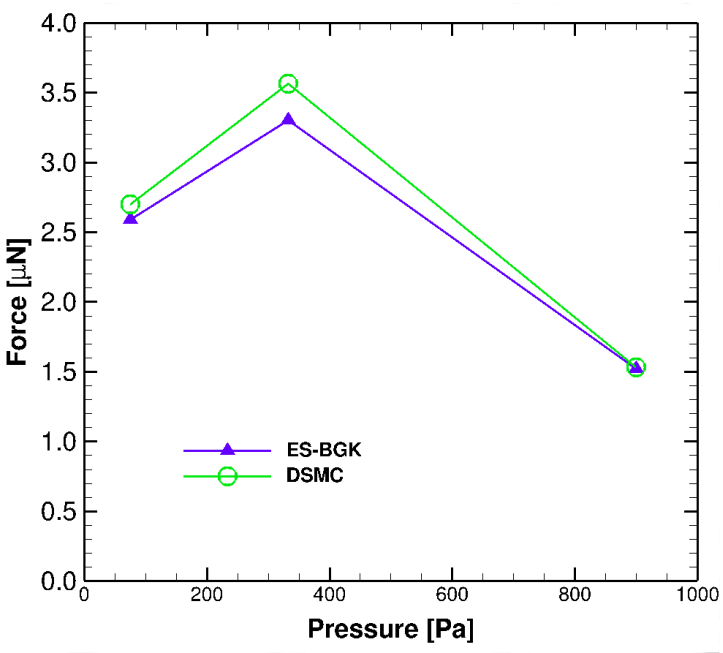

Fig. 5.12.: Force comparison of ESBGK and DSMC

6. MIKRA GEN2

A version of this chapter has been published in Vacuum 161 (2019): 130-137 [11].

Following a successful demonstration of the MIKRA sensor, a new device, MIKRA Gen2 (Figure 6.1), has been developed to improve pressure measurement fidelity of the system. The MIKRA Gen2 sensor operation is identical to that of the first MIKRA, but there are geometrical differences. A silicon dioxide layer between the heater beam and substrate reduces heat loss through the substrate. As the filament is heated, the shuttle arms are displaced in response to the Knudsen forces, the magnitude of which is dependent on the ambient temperature, pressure, and composition.

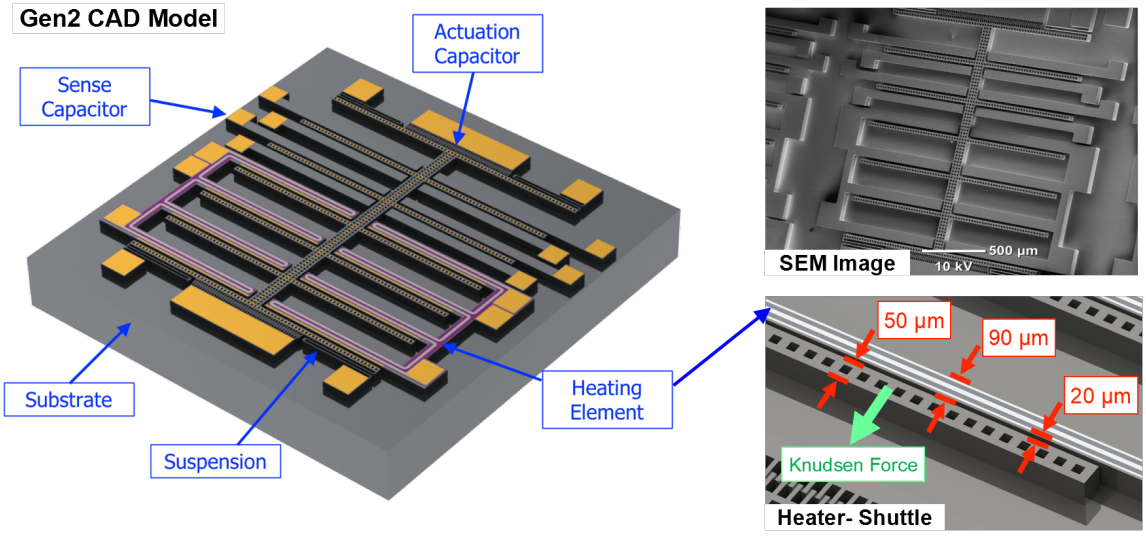

Fig. 6.1.: CAD representation and SEM images of MIKRA Gen2 device.

The Gen2 device operates under the same thermostress convection principles as Gen1 with minor modifications to the heater geometry, suspension, and displacement sensing mechanism. These respective geometrical changes in the beams are shown in

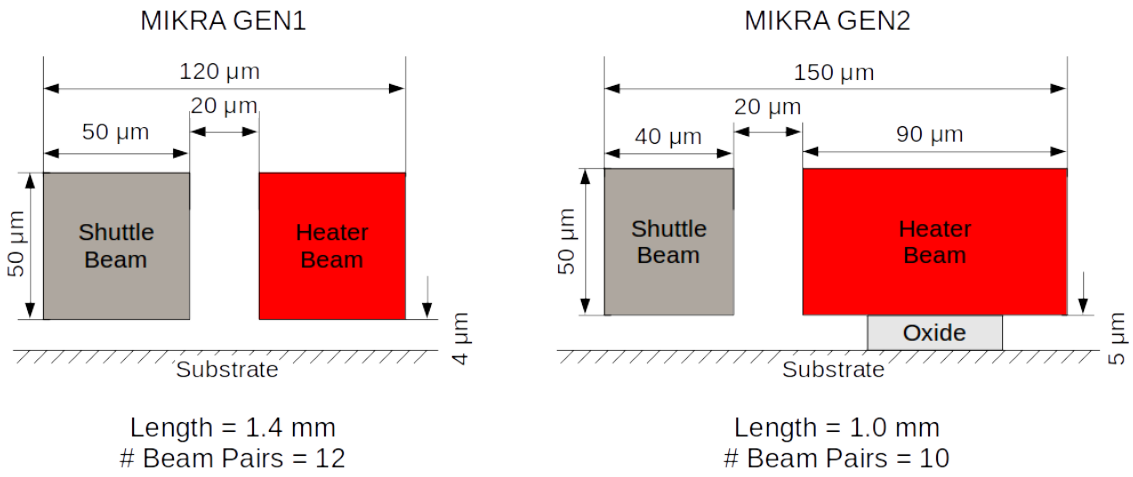

Fig. 6.2.: Geometrical differences between MIKRA Gen1 and Gen2 beams.

Figure 6.2. In the Gen2 device, the heater arms have been widened by 40 micrometers. For reduced power consumption and enhanced measurement sensitivity the number of heating arms was reduced to 10.

7. VERIFICATION AND VALIDATION

A version of this chapter has been published in Vacuum 161 (2019): 130-137 [11].

Before proceeding to the simulations of the new MIKRA concept, we need to complete the validation process for DSMC for the flow conditions applicable here. The forces were previously validated, as they were compared to experimental results. The flowfields were also validated, as very good agreement between DSMC and DGFS were observed. However, DSMC's ability to accurately reproduce the heat flux between the gas and beams for both N_2 and H_2O is of interest here. To do this, we setup standard 1-D Fourier flow DSMC simulations to extract the effective gas thermal conductivity (k) for $Kn_G = \lambda/G$ values equal to 0.01, 1, and 100, where G is the distance between walls. These DSMC results are then compared to the corresponding theoretical and empirical predictions.

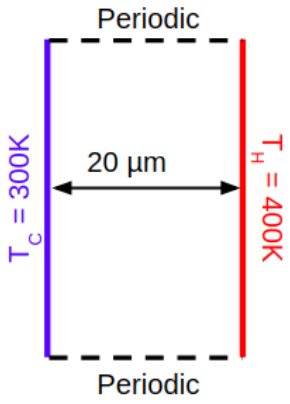

Fig. 7.1.: 1-D Fourier flow simulated conditions.

A schematic of the DSMC domain and boundary conditions for the this set of validation cases is given in Fig. 7.1. The gap distance G between the cold (300 K)

and hot (400 K) walls, is the same as the gap between MIKRA beams (20 μm). Table 7.1 lists the collision model parameters used for this validation study. Since we are simulating a mixture here, VSS was the collision model used. Note that for collisions between different species (N_2-H_2O), the average of the model parameters is used. The DSMC results for the wall heat fluxes for pure nitrogen and water vapor cases are summarized in Table 7.2. The effective thermal conductivity, based on the continuum Fourier equation (Eq. 7.1), is also provided.

$$k^{DSMC} = \frac{q^{DSMC}}{T_H - T_C} G. \tag{7.1}$$

The ratio q_{N_2}/q_{H_2O} ranges from 1.08 in continuum to 1.32 in the free molecular regime. This shows us that despite the extra rotational degree of freedom in H_2O molecules, N_2 still has a larger heat flux.

Table 7.1.: VSS model parameters (at $T_{ref} = 273$ K) and number of rotational degrees of freedom (DOFs) [37], [38]

	N_2	H_2O
Reference diameter, d_{ref} (Å)	4.07	5.78
Viscosity index, ω (-)	0.74	1.00
Scattering parameter, α (-)	1.36	1.00
Rotational #DOFs, ζ_R (-)	2	3

The DSMC results (Table 7.2) now have to be compared to theoretical results. The theory of transport coefficients for monatomic dilute gases at thermal equilibrium is known [4]. Molecules with internal degrees of freedom, however, are more complicated, and either phenomenological models or empirical data is usually required. In order to validate our DSMC calculations, the heat flux q^{DSMC} values for the con-

Table 7.2.: DSMC-predicted heat fluxes q^{DSMC} and effective gas thermal conductivities k^{DSMC} based on 1-D Fourier flows.

$Kn_G = \lambda/G$	$q_{N_2}^{DSMC}$	$q_{H_2O}^{DSMC}$	$k_{N_2}^{DSMC}$	$k_{H_2O}^{DSMC}$
(-)	(W/m^2)	(W/m^2)	(mW/m/K)	(mW/m/K)
0.01	137,779	127,422	27.6	25.5
1	26,953	19,885	5.49	3.98
100	372	258	0.074	0.056

tinuum regime ($Kn_G = 0.01$) are compared to those obtained by using Eucken's approximation (Eq. 7.2), and a modified Eucken's approximation (Eq. 7.3) [39] .

$$k^{Eucken} = \frac{(9\gamma - 5)\ c_v}{4}\ \mu, \tag{7.2}$$

$$k = \frac{5}{2}\left[1 - \left(1 - \frac{2}{5}\frac{\rho D}{\mu}\right)\left(\frac{5}{2} - \frac{3}{2}\gamma\right)\right]\ \mu c_v \tag{7.3}$$

where γ is the ratio of specific heats (c_p/c_v), μ is the dynamic viscosity, ρ is the density, and D is the self-diffusion coefficient (Eq. 7.4) [26].

$$D^{VSS} = \frac{3\mu\alpha}{5\rho}\left[\frac{7 - 2\omega}{2 + \alpha}\right] \tag{7.4}$$

By substituting Eq. 7.4 into Eq. 7.2, we obtain Eq. 7.5.

$$k = \frac{5}{2}\left[1 - \left(1 - \frac{6\alpha}{25}\frac{(7 - 2\omega)}{2 + \alpha}\right)\left(\frac{5}{2} - \frac{3}{2}\gamma\right)\right]\ \mu c_v \tag{7.5}$$

A more advanced expression for thermal conductivity of polyatomic gases is further derived in [39] with rotational relaxation time. However, it requires high fidelity assumptions about the relaxation of H_2O.

In the equations above, c_p and c_v are the specific heats, which are simply given by classical kinetic theory

$$c_p = \frac{(5+\zeta_R)}{2}\ R \qquad\qquad c_v = \frac{(3+\zeta_R)}{2}\ R, \tag{7.6}$$

and only depend on the active DOFs (rotational in this case) and molecular mass m via the specific gas constant $R = k_B/m$. For consistency, μ is calculated according to the VSS model

$$\mu^{VSS} = \frac{5(\alpha+1)(\alpha+2)\sqrt{mk_BT_{ref}}}{4\sqrt{\pi}\alpha(5-2\omega)(7-2\omega)d_{ref}^2}. \tag{7.7}$$

Similarly, the following analytical expression can be used to calculate the conductive heat transfer for the free molecular case ($Kn_G = 100$)

$$q^{FM} = nk_B\sqrt{\frac{2RT_HT_C}{\pi}} * (\sqrt{T_H} - \sqrt{T_C}) * [2 + \frac{5-3\gamma}{2(\gamma-1)}]. \tag{7.8}$$

Table 7.3.: DSMC-predicted heat fluxes q^{DSMC} and effective gas thermal conductivities k^{DSMC} based on 1-D Fourier flows.

$Kn_G = \lambda/G$	$q_{N_2}^{DSMC}/q_{N_2}^{Theory}$	$q_{H_2O}^{DSMC}/q_{H_2O}^{Theory}$
(-)	(-)	(-)
0.01	1.08	1.18
100	1.014	1.00

The ratio of DSMC to these theoretical results for the Fourier heat fluxes are listed in Table 7.3. Note that both Eucken's approximation and the modified Eucken's approximation produced very similar results and the change in the ratio was within 2%. The overall agreement between DSMC and theory is acceptable for MIKRA characterization given that the results for $Kn_G = 0.01$ rely on Eucken's approximation and that uncertainties on MIKRA experimental data for such a flow regime is in the range of $\pm 15\%$.

While we know that DSMC can predict conduction heat fluxes within an acceptable accuracy, convection also plays a key role in the MIKRA flowfield structure. Convection depends strongly on the flow geometry, and is therefore quanitified in terms of empirical correlations for the heat transfer coefficient h and is calibrated to a certain range of dimensionless flow parameters [40]. Newton's law of cooling tells us the convective heat flux is:

$$q = h\,(T_H - T_C). \tag{7.9}$$

To the best of the author's knowledge, there are no correlations for h that are applicable in MIKRA simulations, with rarefied and low speed flows around rectangular cross-sections. Therefore the goal here is to find empiral data for a case and estimate the ratio of the convective heat transfer coefficients for N_2 and H_2O gas flows in continuum.

Based on the experimentally calibrated correlation for the Nusselt number Nu in flow over a horizontal cylinder of diameter D [41], the heat transfer coefficient can be obtained from

$$Nu = \frac{h\,D}{k} = 0.32 + 0.43\,Re_D^{0.52}, \tag{7.10}$$

where $Re_D = \rho U D/\mu$ and U is the for the flow velocity. This expression is valid for $Re_D > 0.1$ and $Kn \ll 1$. To meet both requirements, a Knudsen number of 0.01 was chosen along with a flow speed (V) of 1 m/s and cylinder diameter (D) of 100 μm. The Reynolds numbers (Re_D) for N_2 and H_2O are equal to 0.359 and 0.225, respectively. If we take these Re_D values and the thermal conductivities from Table 7.2, we can estimate h from Eq. (7.10). The corresponding h_{N_2}/h_{H_2O} ratio is 1.38.

The test cases for both convection and conduction suggest that we should see a higher heat flux in flows dominated by N_2 rather than H_2O. Also, we can rely on the heat flux results from DSMC, as it was validated through the Fourier flow test case.

8. NUMERICAL METHODS: MIKRA GEN2

A version of this chapter has been published in Vacuum 161 (2019): 130-137 [11].

The numerical parameters are very similar as the simulations in Gen1. 2-D simulations were deemed appropriate here. The boundary conditions are shown in Fig. 8.1. The only difference between the boundary conditions here and those in MIKRA Gen1 are the shuttle and heater beam geometries. The freestream conditions, DSMC and simulation parameters, and boundaries are the same. This set of numerical parameters and boundary conditions can reproduce the experimental data on Knudsen forces [20]. Therefore, we use the same values for the present heat dissipation study of the MIKRA Gen2 device. The flow conditions investigated in this work are the same for MIKRA Gen1 previous studies [20]. The specific freestream temperatures T_∞, pressures p_∞ and heater and shuttle beam temperatures, T_H and T_C, are listed in Table 8.1. The beam temperatures rely on MIKRA Gen1 experimental data at 100 mW of total power dissipation and corresponding Knudsen values are based on the gap between beams, i.e., $Kn_G = \lambda/G$. The DSMC framework, kinetic data, and collision model parameters are the same used in the heat flux verification chapter. Note one key difference between the MIKRA Gen1 and Gen2 simulations is that VHS was used in Gen1. However, as we consider mixtures now, VSS is the appropriate model here.

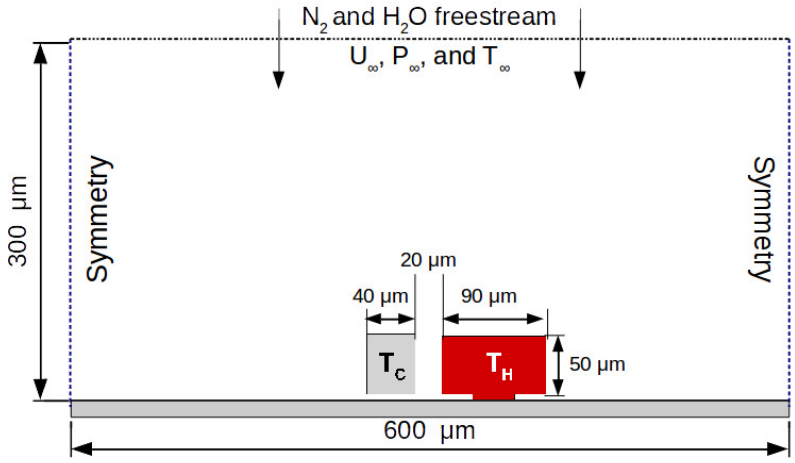

Fig. 8.1.: MIKRA Gen2 simulated domain and boundary conditions.

Table 8.1.: MIKRA Gen2 investigated freestream and beam conditions.

p_∞ (Torr)	$Kn_G^{N_2}$ (-)	$Kn_G^{H_2O}$ (-)	T_C (K)	T_H (K)
0.188	11.49	5.50	306	370
0.465	4.64	2.22	306	370
1.163	1.85	0.89	306	363
2.903	0.74	0.36	306	356
7.246	0.30	0.14	304	331

9. MIKRA GEN2 RESULTS AND DISCUSSION

A version of this chapter has been published in Vacuum 161 (2019): 130-137 [11].

9.1 Knudsen Force for N_2-H_2O Mixtures

Although the MIKRA Gen2 study considers the same total pressures and temperatures covered in MIKRA Gen1 simulations, we investigated N_2, H_2O vapor, and 50/50 N_2-H_2O gas mixtures instead of pure N_2 and He.

Figures 9.1 and 9.2 show the speed flowfields within the MIKRA Gen2 device for a 100% N2 mixture, while figures 9.3 and 9.4 show the speed flowfields for a 100% H2O mixture. Once again we see the nonintuitive flow structure in this vortex dominated flow. The vortices within the gap contribute to the Knudsen force. The larger heater in the Gen2 configuration contributes to a higher velocity over the shuttle.

Figures 9.5 and 9.6 show the near beam flowfields of temperature for all five pressure cases for both the 100% N2 and H2O case sets. In general, as the ambient pressure increases, the temperature contour over the top increases. Note that that pattern doesn't continue for the highest pressure case due to the much lower heater beam temperature. The pattern is further exaggerated in the H2O dominated flow.

Figures 9.7 and 9.8 compare the near-beam flowfields for Gen1 and Gen2 cases at $p_\infty = 1.163$ Torr, i.e., $Kn_G^{N_2} = 1.85$ and $Kn_G^{H_2O} = 0.89$. Here it's clear that under the same conditions, the velocity is larger over the shuttle in Gen2. We also see that more H2O in the flowfield results in a larger velocity. The temperature flowfield shows the larger contour over the top face in Gen2 as compared to Gen1, which is expected due to the increased size. As more H2O is added to the flowfield, we see that contour over the top increase further.

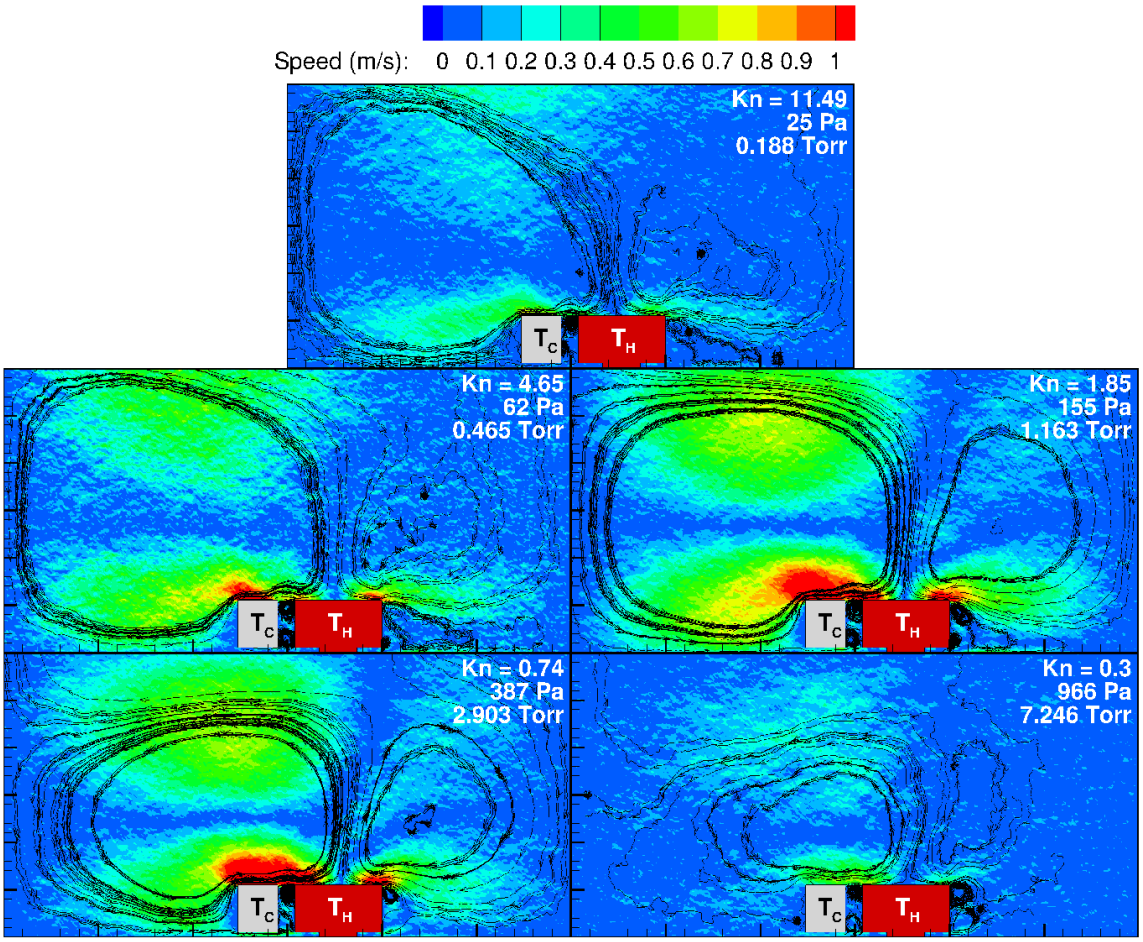

Fig. 9.1.: Speed flowfield of MIKRA Gen2 for all five pressures with 100% N2.

Figure 9.9 compares the respective DSMC measured Knudsen forces on the shuttle beam for MIKRA Gen2 along with previous Gen1 numerical and experimental data. These simulations show that the peak force for MIKRA Gen2 also occurs at $Kn_G \sim 1$ with respect to the gap. Gen2 experiences smaller forces due to the shorter beams and reduced number of heater-shuttle beam pairs compared to Gen1. For the same pressure, the forces produced in pure H_2O vapor cases are lower than for pure N_2. However, the graph shows that at low Knudsen numbers, H_2O vapor has a larger force for similar Knudsen numbers.

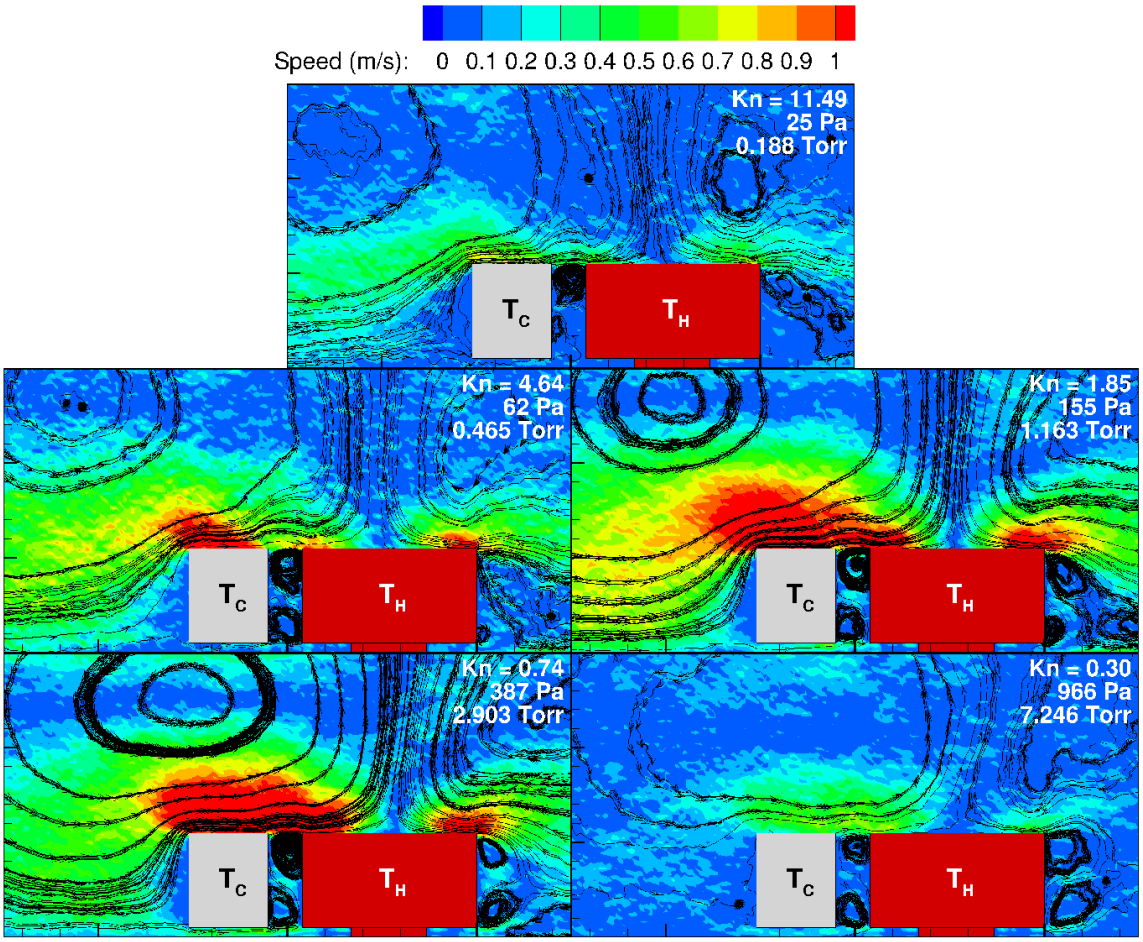

Fig. 9.2.: Near beam view of speed flowfield of MIKRA Gen2 for all five pressures with 100% N2.

A dimensionless formula to predict the Knudsen force based on ambient pressure and concentrations of N_2 and H_2O vapor is proposed here. As shown in Fig. 9.10, the force decreases with the water vapor concentration such that for N_2-H_2O mixtures it can be expressed as

$$F_{mix} = F_{N2} + SX_{H2O} \tag{9.1}$$

where F_{N2} represents the force in a pure N_2 system at the same pressure as the mixture, X_{H_2O} is the concentration of H_2O vapor, and S is the slope of each line in

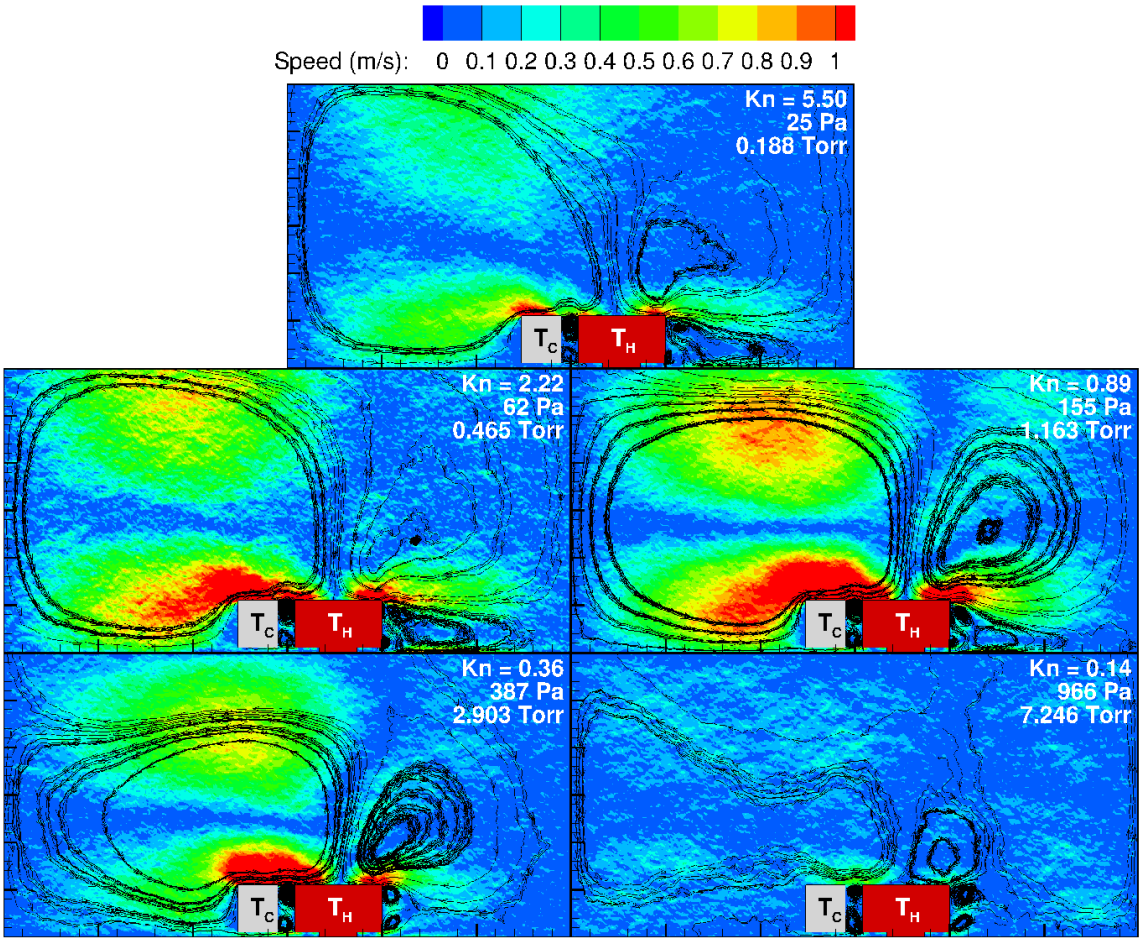

Fig. 9.3.: Speed flowfield of MIKRA Gen2 for all five pressures with 100% H2O.

Fig. 9.10. Note that Eq. (9.1) is only valid for the specific beam temperatures listed in Table 4.2, which should be reproduced whenever the dissipated heater beam power is $\sim$ 100 mW. The following $S(Kn_G^{N_2})$ fitting function is proposed to calculate the slope of each line shown in Fig. 9.10.

$$S = aKn_G^{N_2} \exp(bKn_G^{N_2}) \tag{9.2}$$

where Kn_{N2} is the Knudsen number for the pure N_2 case, $a = -1.52$ and $b = -1.03$. Fig. 9.11, which is plotted in terms of $F_{mix} - F_{N_2}$, shows us that the linear fit captures

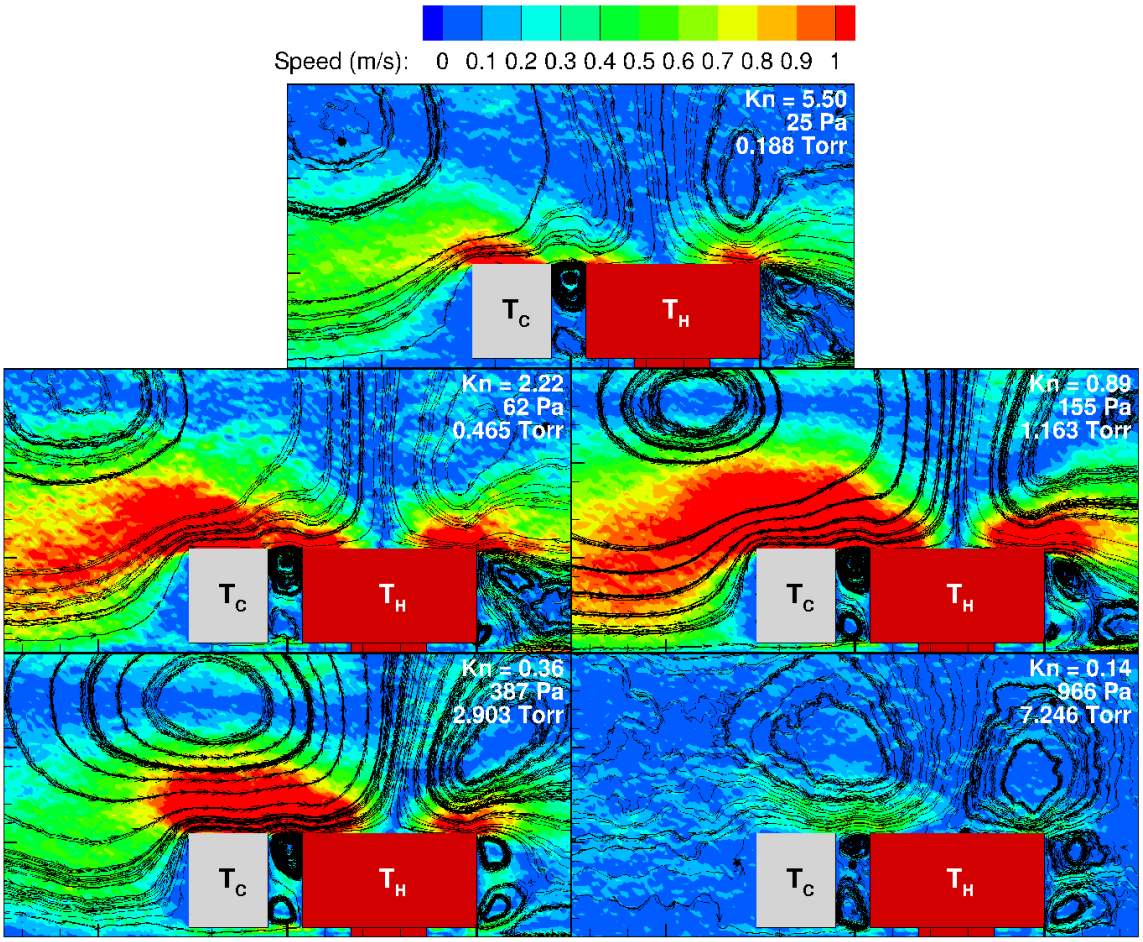

Fig. 9.4.: Near beam view of speed flowfield of MIKRA Gen2 for all five pressures with 100% H2O.

the DSMC results. This means if we know only F_{N_2} at a given pressure and $Kn_G^{N_2}$, we can predict the MIKRA Gen2 Knudsen forces for any N_2-H_2O concentration at the same pressure.

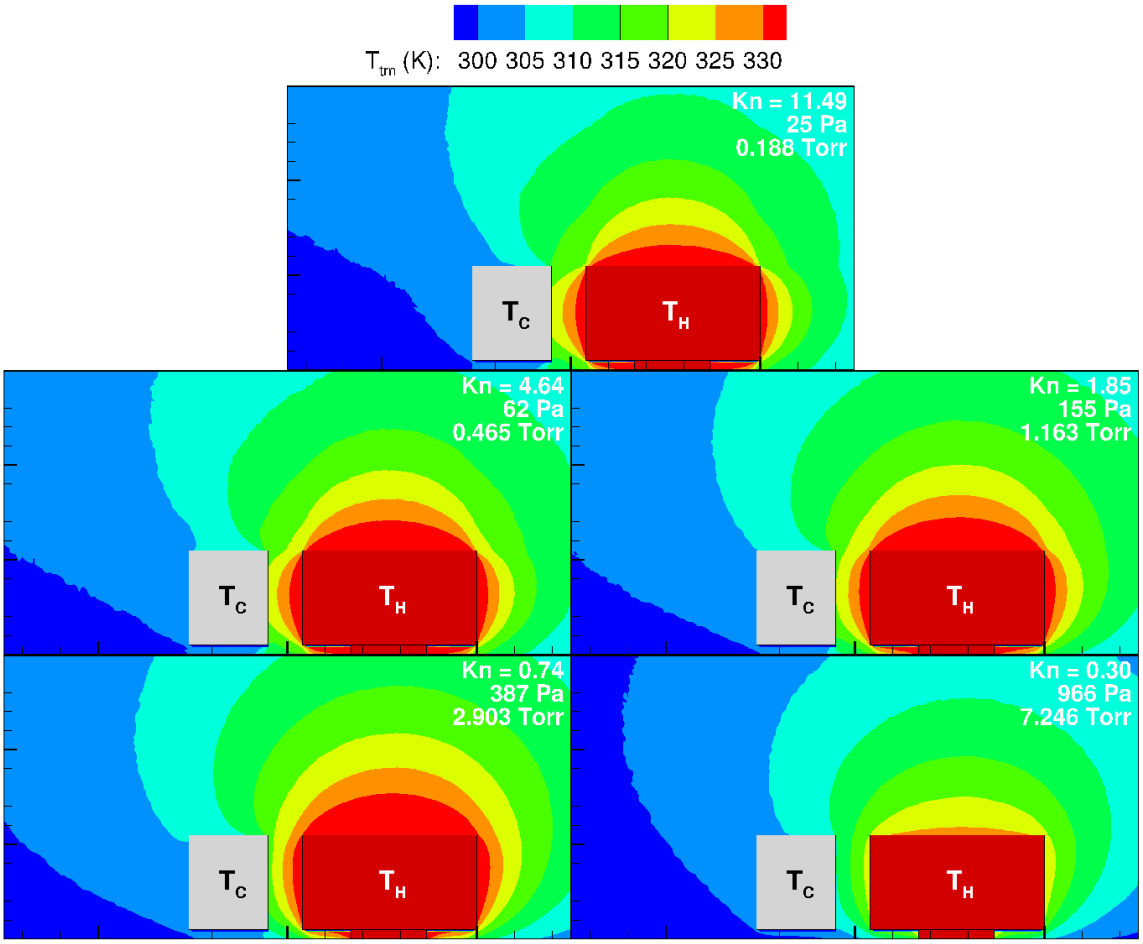

Fig. 9.5.: Near beam view of temperature flowfield of MIKRA Gen2 for all five pressures with 100% N2.

9.2 Species Separation

Large thermal gradients can also cause species separation. Figure 9.12 shows that MIKRA causes slight separation in N_2-H_2O mixtures. The concentration of N_2 is lower around the heater beam for the higher pressures simulated. However, the difference in concentration is less than 0.2%, suggesting a limited application within

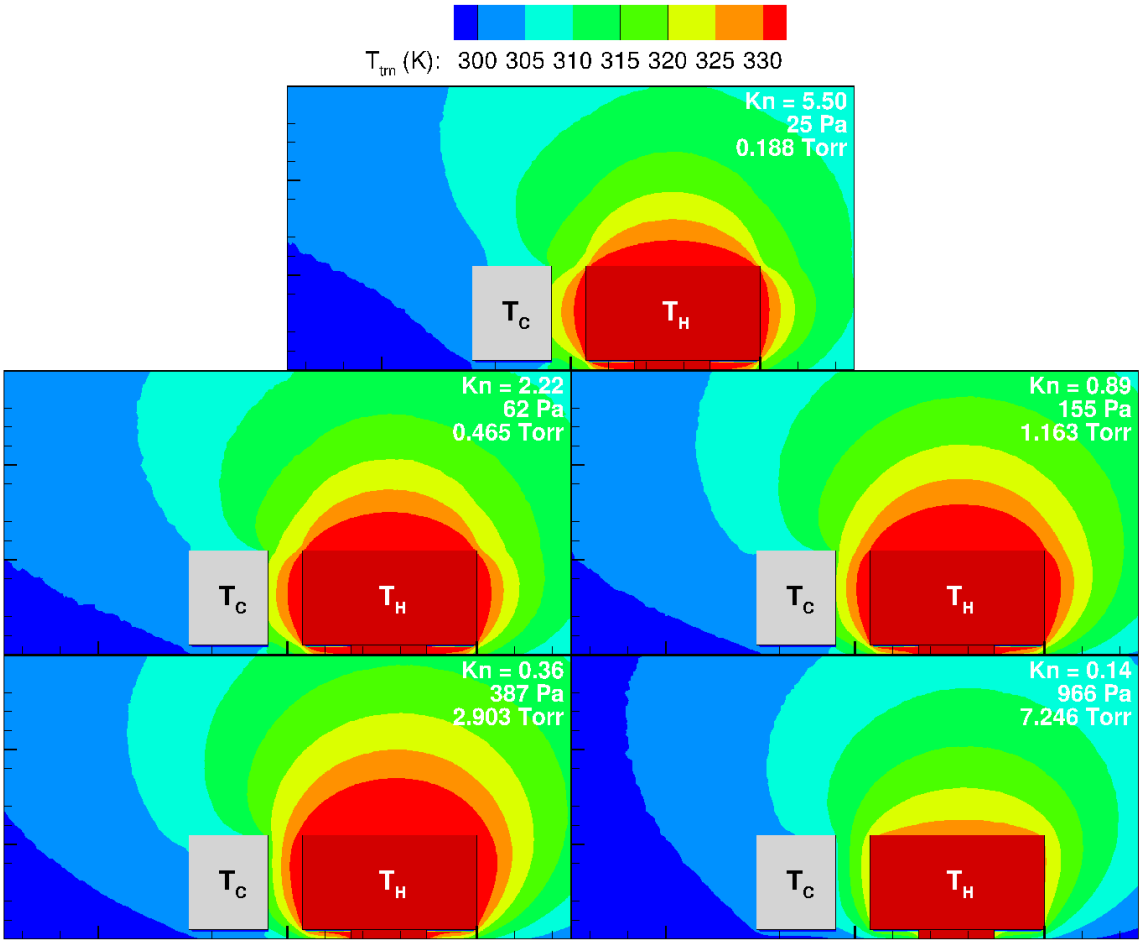

Fig. 9.6.: Near beam view of temperature flowfield of MIKRA Gen2 for all five pressures with 100% H2O.

this setup. That being said, it might be possible to design a microscale device to increase species mixing or separation using thermal gradients.

9.3 Gap Variation

The gap size between the heater and shuttle beams is another interesting design aspect, as any change in geometry changes the Knudsen force. MIKRA Gen1 ex-

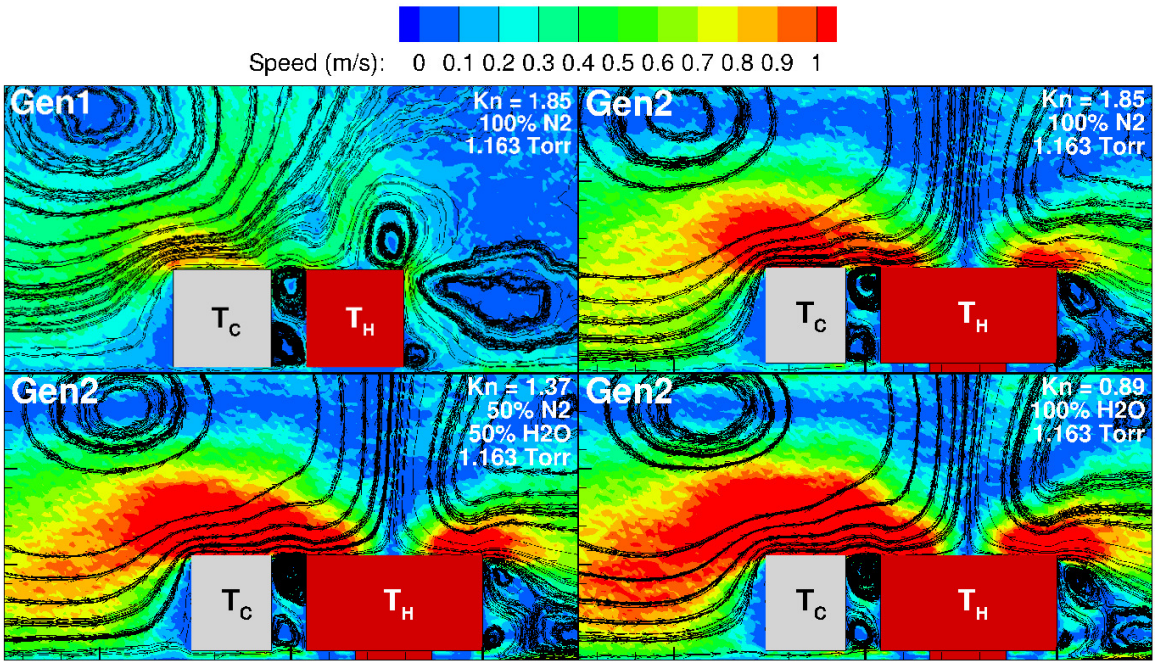

Fig. 9.7.: Speed flowfield of MIKRA Gen1 and Gen2 configurations.

periments and all simulations told us that the peak force was around a Kn_G of one. Figure 9.13 shows, however, that for a fixed pressure and temperature condition the force monotonically increases with a decreasing gap G, and the decreasing gap size correlates to an increase in Kn_G. We can normalize the force based on Knudsen number ($F(Kn)$) to recover a maximum force at the same Knudsen number regardless the gap size by proposing to define a new Knudsen number Kn_L, where $L = G + 130$ μm, or the total distance from the left side of the shuttle to the right side of the heater (Fig. 6.2). With this new definition of Knudsen number, the force peaks at the same $Kn_L \sim 0.1 - 0.2$ value as demonstrated in Fig. 9.14.

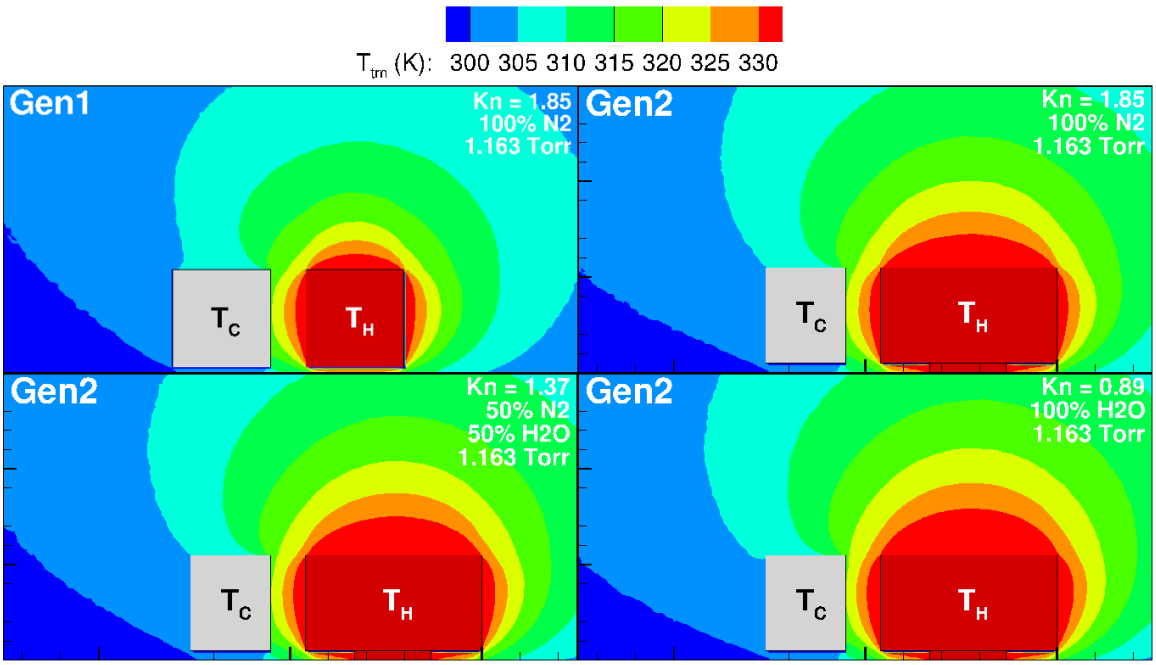

Fig. 9.8.: Temperature flowfield of MIKRA Gen1 and Gen2 configurations.

9.4 Heater Beam Power Dissipation

The total heat flux exchanged between the gas and the heater beam is another important MIKRA process parameter that can be calculated in these simulations. In DSMC, the heat flux q is calculated by the net energy flux of molecules colliding with the panel elements which make up the surface. The net heat flux is related to the sum of the energies (translational and rotational in this case) of both the incident and reflected molecules,

$$q = \frac{W_p}{A\,\Delta t} \sum_{j=1}^{N} (\frac{mc^2}{2} + \varepsilon_R)_i - (\frac{mc^2}{2} + \varepsilon_R)_r \tag{9.3}$$

where c is the molecular speed, ε_R is the rotational energy, and W_p is number of real particles represented by each of the N computational particles colliding with each panel of area A within each time step Δt. The subscripts (i) and (r) mean incident and reflected molecules, respectively.

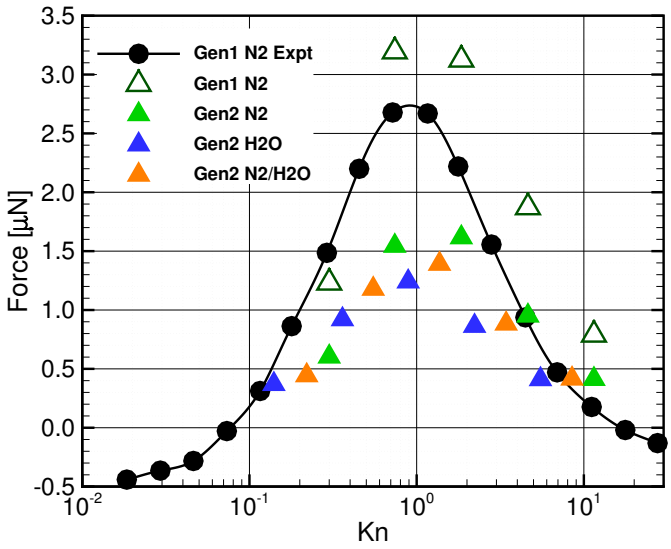

Fig. 9.9.: Comparison of Knudsen forces as a function of Kn_G for Gen1 experiments (solid line) and simulations (empty symbols), and Gen2 simulations (filled symbols) for gas compositions.

In order to generalize the heat flux data obtained from DSMC for a single MIKRA heater beam, Eq. (9.3) results are normalized by dividing the heat flux by the temperature gradient to obtain the heat transfer coefficient: $h = q/\Delta T$, where ΔT is the difference in temperature between the shuttle and heater beams. As expected, the heat flux coefficient increases with pressure (Figure 9.15). We see that, by comparing the pure N_2 cases, MIKRA Gen2 has a higher heat flux than Gen1. This means that if the same power is required for both devices, Gen2 is more efficient. The oxide layer in the Gen2 configuration (Fig. 6.2) reduces the heater-to-substrate dissipation, which is a major contributor to the total heat flux [20], the wetted area of the Gen2 heater beam is $\sim$20% greater than in Gen1. This ratio is similar to the observed difference between the respective h values. For the same pressure, H_2O has a higher heat flux than N_2. However, the graph shows that for similar Knudsen numbers, N_2 has a larger heat flux. This qualitatively agrees with an earlier discussion which shows that

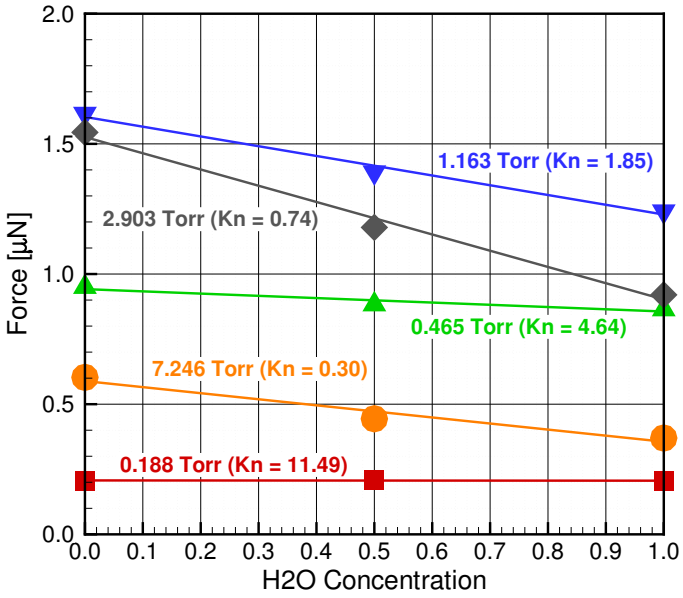

Fig. 9.10.: Force versus H_2O concentration.

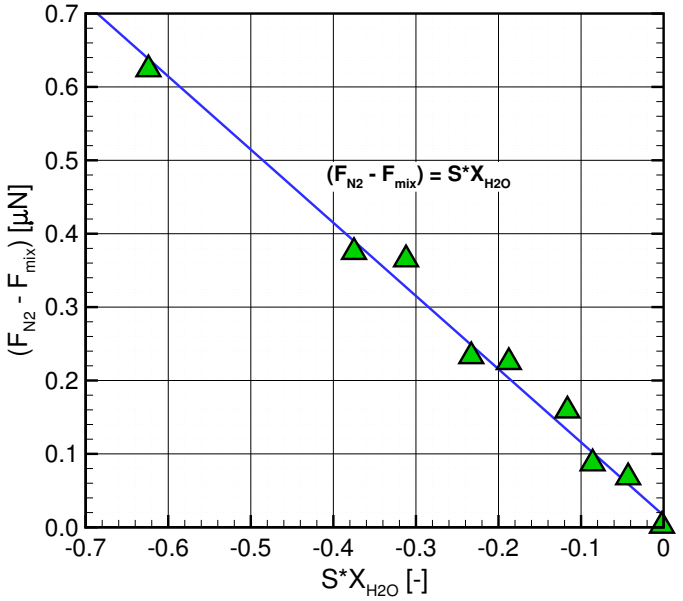

Fig. 9.11.: Proposed linear fit for F_{mix} results.

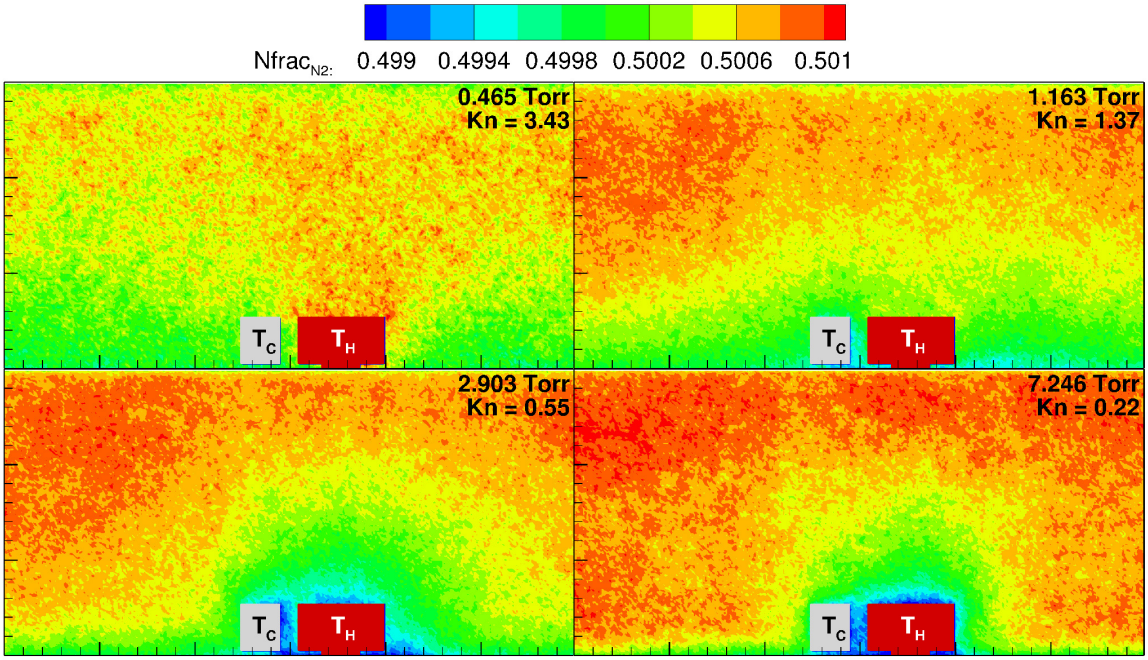

Fig. 9.12.: Concentration of N_2 for different pressures.

the total heat flux is slightly larger for N_2 in the continuum and free molecular limits. The results of Gen1 are also compared to the heat transfer coefficient computed in Gallis et. al. [42]. There is good agreement for free molecular flows.

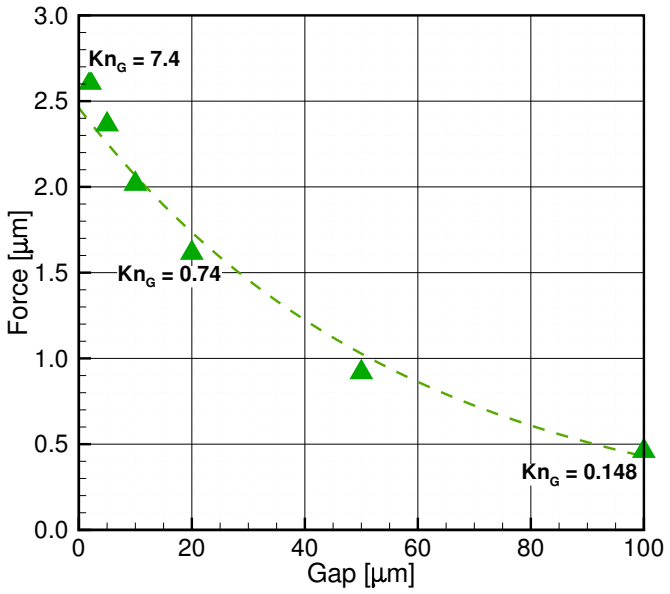

Fig. 9.13.: Gap variation effect at 2.9 Torr.

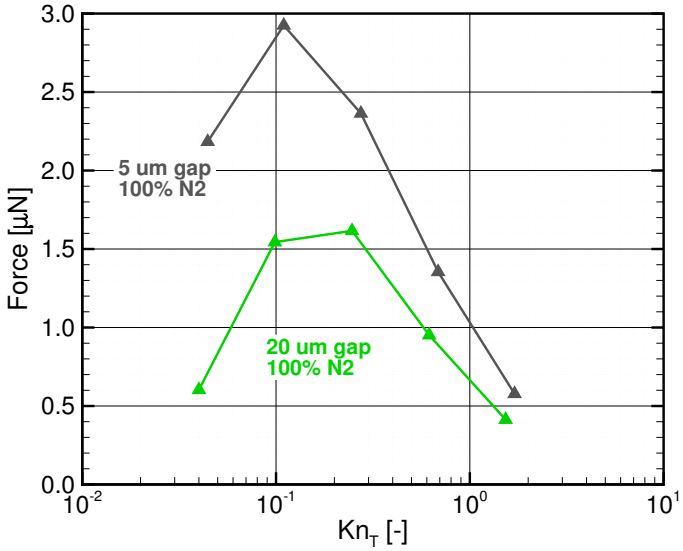

Fig. 9.14.: Force vs. Kn_L

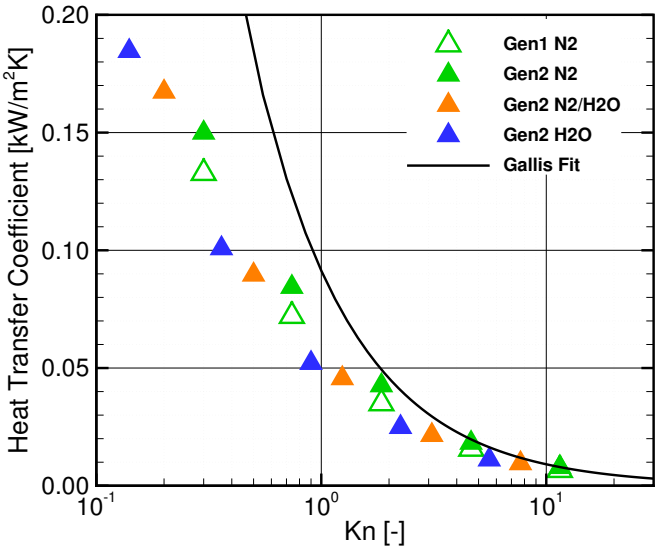

Fig. 9.15.: DSMC predicted heat transfer coefficients h for heater beam power dissipation.

10. SUMMARY

A MEMS based gas pressure and composition sensor that exploits thermostress convection known as the Microscale In-Plane Knudsen Radiometric Actuator (MIKRA) was developed and characterized with experimental measurements and numerical methods. MIKRA is a low power and compact sensor that offers high-resolution spatial mapping of flow properties in vacuum-based manufacturing environments such as lyophilization chambers. It uses in-plane motion of a shuttle beam set in response to Knudsen forces that develop due to thermostress convection. These Knudsen forces are formed between a heated and the shuttle beams causing the shuttle beams to move away from the heaters. Shuttle movement is measured by comb capacitors. MIKRA reveals the bimodal nature of Knudsen forces with respect to pressure, which has also been observed previously many times. MIKRA also shows how sensitive the force is to gas composition.

The rarefied conditions within the MIKRA sensor make the direct simulation Monte Carlo (DSMC) method appropriate. DSMC can not only measure the Knudsen forces within the sensor, but can also measure the heat flux from the gas to solid beam interaction as well as flowfield mapping, both of which are not feasible experimentally.

DSMC proved to be a reliable method for simulating these flows, as the force measurements agreed with those from experiments. Both conclude that the Knudsen force peaks at a Knudsen number of 1 with respect to the gap. DSMC was also compared to other numerical methods for further validation. ESBGK and DGFS are two numerical methods that solve the Boltzmann equation differently than DSMC, making them good validation tools. We see the flowfields and forces are similar between DSMC and the other numerical methods. Therefore, we can conclude that DSMC is a reliable tool to simulate such flows.

After a successful demonstration of DSMC's ability to simulate MIKRA Gen1, DSMC was used to simulate a new version of MIKRA called MIKRA Gen2, that had some geometrical changes. For Gen2 simulations, we were also interested in N_2-H_2O mixtures. The force was very sensitive to the mixture, and a correlation was proposed to predict the forces in such mixtures. We also see that the total heat flux dissipation is higher in mixtures dominated by N_2 instead of H_2O vapor. DSMC can play a vital role in the study of these flows, as well as future design iterations of MIKRA.

Future work includes making higher fidelity simulations. Although DSMC force results shows good agreement with experimental results qualitatively, there were some key features that the DSMC simulations didn't include, such as 3D effects, coupling effects with multiple beams, and temperature nonuniformities within the beams themselves. Therefore, should the computational resources be available, future work can include a high fidelity 3D simulation of the full MIKRA device that would fix all three of these short comings.

Another point of interest throughout this work is thermal diffusion, or species separation by thermal gradients. This work shows that MIKRA is not effective for mixture separation or mixing, however MEMS devices might be able to use thermal gradients to separate or mix species. Therefore, future work can also include finding concepts where thermal diffusion is significant.

REFERENCES

REFERENCES

[1] W. Crookes, "On attraction and repulsion resulting from radiation," *Philosophical transactions of the Royal society of London*, vol. 164, pp. 501–527, 1874.

[2] M. Knudsen, "Thermischer molekulardruck der gase in röhren," *Annalen der Physik*, vol. 338, no. 16, pp. 1435–1448, 1910.

[3] A. Passian, R. Warmack, T. Ferrell, and T. Thundat, "Thermal transpiration at the microscale: a Crookes cantilever," *Physical review letters*, vol. 90, no. 12, p. 124503, 2003.

[4] S. Chapman and T. G. Cowling, "The mathematical theory of non-uniform gases: an account of the kinetic theory of viscosity, thermal conduction and diffusion in gases," 1970.

[5] S. Loyalka, "Knudsen forces in vacuum microbalance," *The Journal of Chemical Physics*, vol. 66, no. 11, pp. 4935–4940, 1977.

[6] J. G. Fierro and A. A. Garcia, "Gas dynamics at low pressures in a vacuum microbalance," *Vacuum*, vol. 31, no. 2, pp. 79–84, 1981.

[7] A. Alexeenko, E. P. Muntz, M. Gallis, and J. Torczynski, "Comparison of kinetic models for gas damping of moving microbeams," in *36th AIAA Fluid Dynamics Conference and Exhibit*, 2006, p. 3715.

[8] T. Zhu and W. Ye, "Origin of knudsen forces on heated microbeams," *Physical Review E*, vol. 82, no. 3, p. 036308, 2010.

[9] J. Nabeth, S. Chigullapalli, and A. A. Alexeenko, "Quantifying the Knudsen force on heated microbeams: A compact model and direct comparison with measurements," *Physical Review E*, vol. 83, no. 6, p. 066306, 2011.

[10] Y. A. Anikin, "Numerical study of radiometric forces via the direct solution of the boltzmann kinetic equation," *Computational Mathematics and Mathematical Physics*, vol. 51, no. 7, pp. 1251–1266, 2011.

[11] A. Pikus, I. B. Sebastião, A. Strongrich, and A. Alexeenko, "Characterization of a knudsen force based vacuum sensor for n2h2o gas mixtures," *Vacuum*, vol. 161, pp. 130–137, 2019.

[12] N. Selden, C. Ngalande, N. Gimelshein, S. Gimelshein, and A. Ketsdever, "Origins of radiometric forces on a circular vane with a temperature gradient," *Journal of Fluid Mechanics*, vol. 634, pp. 419–431, 2009.

[13] M. Kogan, V. Galkin, and O. Fridlender, "Stresses produced in gasses by temperature and concentration inhomogeneities. new types of free convection," *Physics-Uspekhi*, vol. 19, no. 5, pp. 420–428, 1976.

[14] V. Galkin and M. Kogan, "Derivation of the equations of slow nonisothermal gas flows," *Fluid Dynamics*, vol. 14, no. 6, pp. 873–880, 1979.

[15] Y. Sone, *Kinetic theory and fluid dynamics*. Springer Science & Business Media, 2012.

[16] E. H. Kennard, *Kinetic theory of gases, with an introduction to statistical mechanics*. McGraw-Hill, 1938., 1938.

[17] M. Kogan, *Rarefied Gas Dynamics*, 1969, vol. 2.

[18] F. Sharipov, *Rarefied gas dynamics: fundamentals for research and practice*. John Wiley & Sons, 2015.

[19] A. Ibrayeva, "Numerical modeling of thermal edge flow," Master's thesis, Purdue University, 2017.

[20] A. Strongrich, A. Pikus, I. B. Sebastião, and A. Alexeenko, "Microscale in-plane Knudsen radiometric actuator: Design, characterization, and performance modeling," *Journal of Microelectromechanical Systems*, vol. 26, no. 3, pp. 528–538, 2017.

[21] N. Gimelshein, S. Gimelshein, A. Ketsdever, and N. Selden, "Impact of vane size and separation on radiometric forces for microactuation," *Journal of Applied Physics*, vol. 109, no. 7, p. 074506, 2011.

[22] A. D. Strongrich, W. J. O'Neill, A. G. Cofer, and A. A. Alexeenko, "Experimental measurements and numerical simulations of the knudsen force on a non-uniformly heated beam," *Vacuum*, vol. 109, pp. 405–416, 2014.

[23] S. Jaiswal, A. A. Alexeenko, and J. Hu, "A discontinuous galerkin fast spectral method for the multi-species full boltzmann equation," *arXiv preprint arXiv:1903.03056*, 2019.

[24] C. Cercignani, *The Boltzmann Equation and Its Applications*. Springer-Verlag, New York, 1988.

[25] S. Harris, *An Introduction to the Theory of the Boltzmann Equation*. Dover Publications, 2004.

[26] G. A. Bird, "Molecular gas dynamics and the direct simulation of gas flows," 1994.

[27] G. Bird, "Approach to translational equilibrium in a rigid sphere gas," *The Physics of Fluids*, vol. 6, no. 10, pp. 1518–1519, 1963.

[28] G. C. Maitland and E. B. Smith, "Critical reassessment of viscosities of 11 common gases," *Journal of Chemical and Engineering Data*, vol. 17, no. 2, pp. 150–156, 1972.

[29] K. Koura, H. Matsumoto, and T. Shimada, "A test of equivalence of the variable-hard-sphere and inverse-power-law models in the direct-simulation monte carlo method," *Physics of Fluids A: Fluid Dynamics*, vol. 3, no. 7, pp. 1835–1837, 1991.

[30] K. Koura and H. Matsumoto, "Variable soft sphere molecular model for inverse-power-law or Lennard Jones potential," *Physics of Fluids A*, vol. 3, no. 10, pp. 2459–2465, 1991.

[31] C. Borgnakke and P. S. Larsen, "Statistical collision model for monte carlo simulation of polyatomic gas mixture," *Journal of computational Physics*, vol. 18, no. 4, pp. 405–420, 1975.

[32] M. A. Gallis, J. R. Torczynski, S. J. Plimpton, D. J. Rader, and T. Koehler, "Direct simulation Monte Carlo: The quest for speed," in *Proceedings of the 29th International Symposium on Rarefied Gas Dynamics*, vol. 1628, no. 1. AIP Publishing, 2014, pp. 27–36.

[33] S. Jaiswal, A. Alexeenko, and J. Hu, "A discontinuous Galerkin fast spectral method for the full Boltzmann equation with general collision kernels," *Journal of Computational Physics*, vol. 378, pp. 178–208, 2019.

[34] I. Gamba, J. Haack, C. Hauck, and J. Hu, "A fast spectral method for the Boltzmann collision operator with general collision kernels," *SIAM J. Sci. Comput.*, vol. 39, pp. B658–B674, 2017.

[35] L. Mieussens, "Discrete-velocity models and numerical schemes for the boltzmann-bgk equation in plane and axisymmetric geometries," *Journal of Computational Physics*, vol. 162, no. 2, pp. 429–466, 2000.

[36] P. Andries, P. Le Tallec, J.-P. Perlat, and B. Perthame, "The gaussian-bgk model of boltzmann equation with small prandtl number," *European Journal of Mechanics-B/Fluids*, vol. 19, no. 6, pp. 813–830, 2000.

[37] K. Koura and H. Matsumoto, "Variable soft sphere molecular model for air species," *Physics of Fluids A: Fluid Dynamics*, vol. 4, no. 5, pp. 1083–1085, 1992.

[38] A. A. Alexeenko, A. Ganguly, and S. L. Nail, "Computational analysis of fluid dynamics in pharmaceutical freeze-drying," *Journal of pharmaceutical sciences*, vol. 98, no. 9, pp. 3483–3494, 2009.

[39] J. Ferziger and H. Kaper, *Mathematical theory of transport processes in gases*. North Holland, 1972.

[40] T. L. Bergman, F. P. Incropera, D. P. DeWitt, and A. S. Lavine, "Fundamentals of heat and mass transfer," 2011.

[41] F. Sauer, "Forced convection heat transfer from horizontal cylinders in a rarefied gas," *Journal of the Aeronautical Sciences*, vol. 20, no. 3, pp. 175–180, 1953.

[42] M. A. Gallis, J. Torczynski, and D. Rader, "A computational investigation of noncontinuum gas-phase heat transfer between a heated microbeam and the adjacent ambient substrate," *Sensors and Actuators A: Physical*, vol. 134, no. 1, pp. 57–68, 2007.

APPENDICES

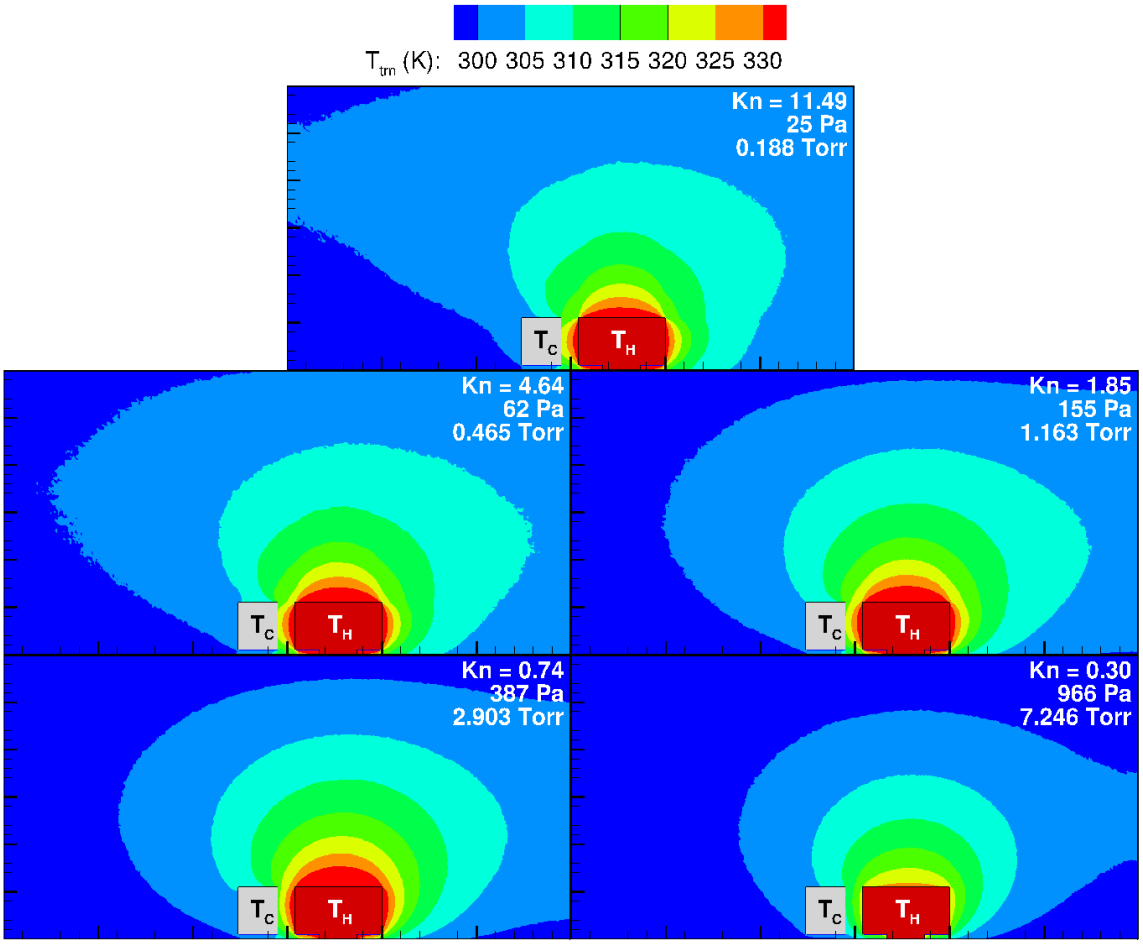

A. 1.: Temperature flowfield of MIKRA Gen2 for all five pressures with 100% N2.

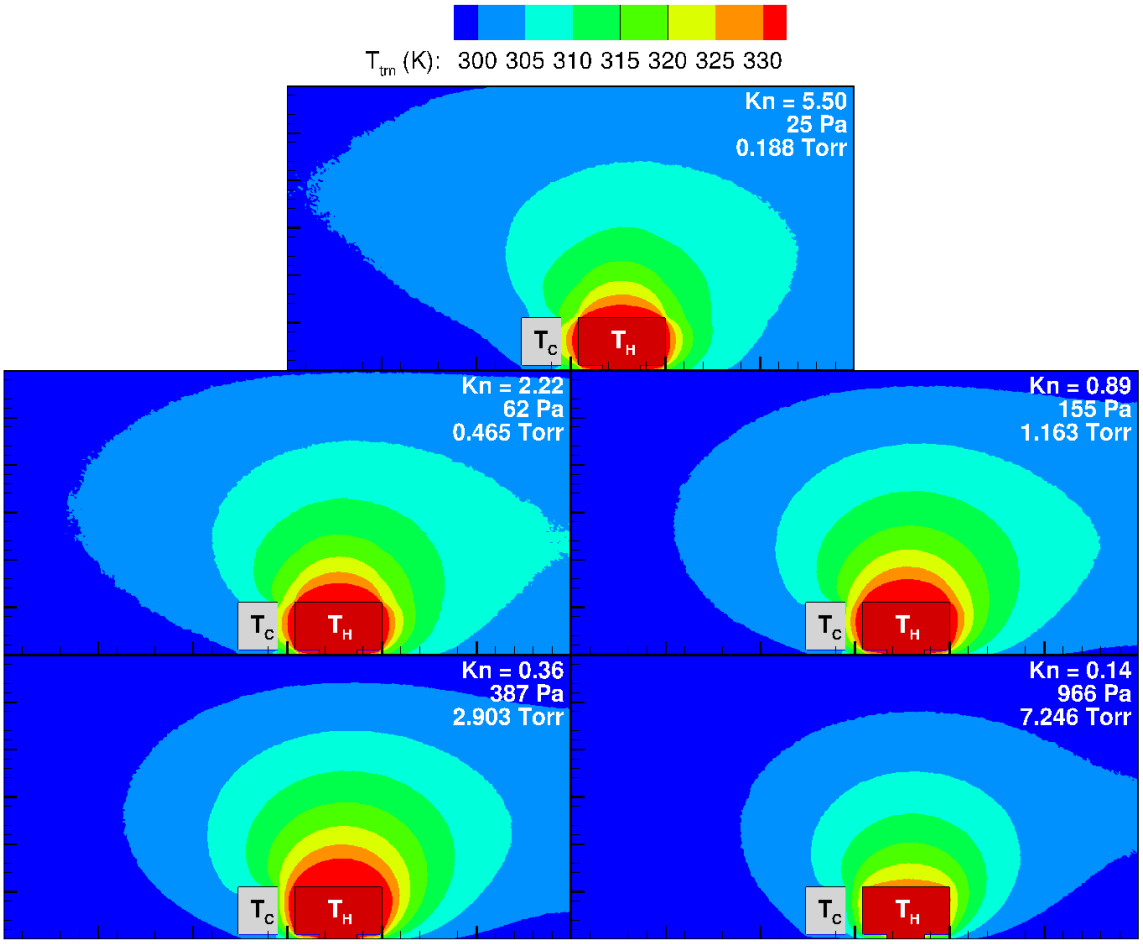

A. 2.: Temperature flowfield of MIKRA Gen2 for all five pressures with 100% H2O.

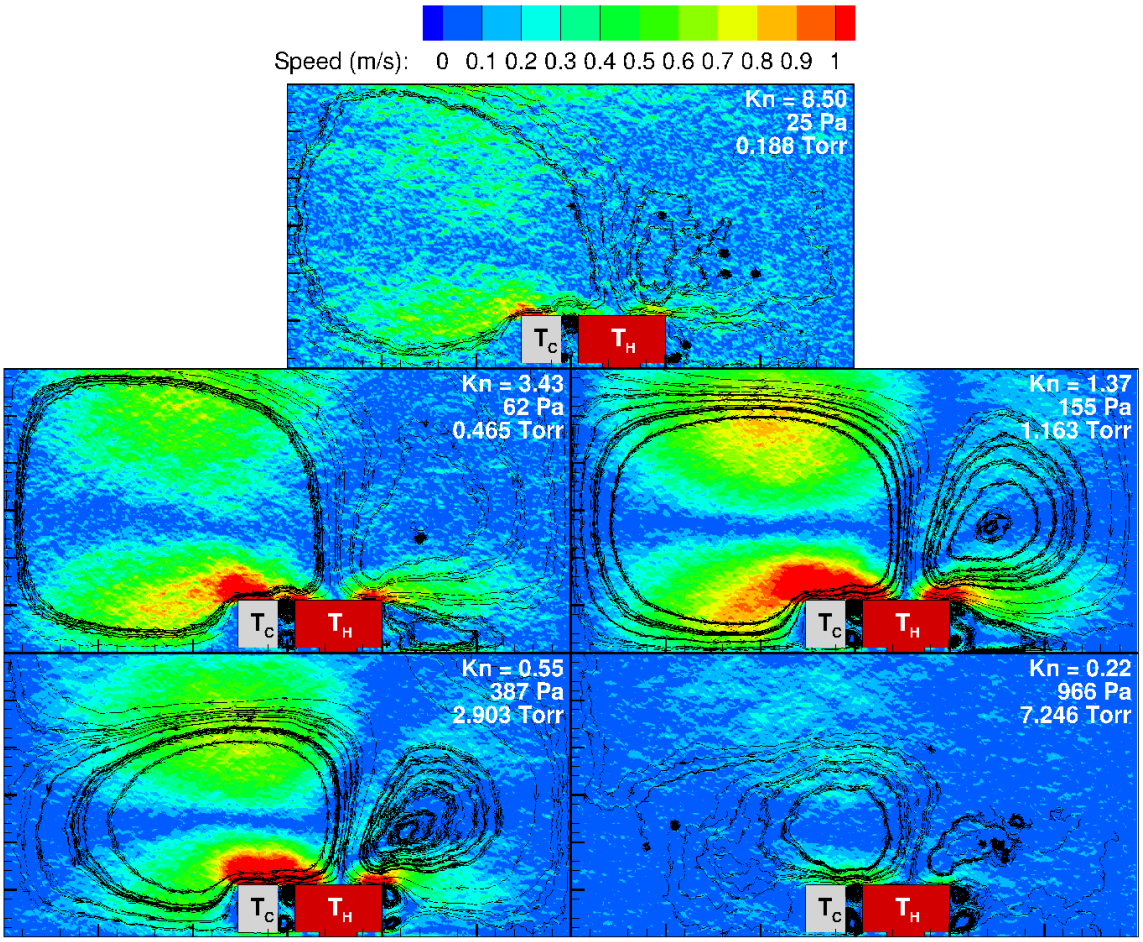

A. 3.: Speed flowfield of MIKRA Gen2 for all five pressures with 50% N2 and 50% H2O.

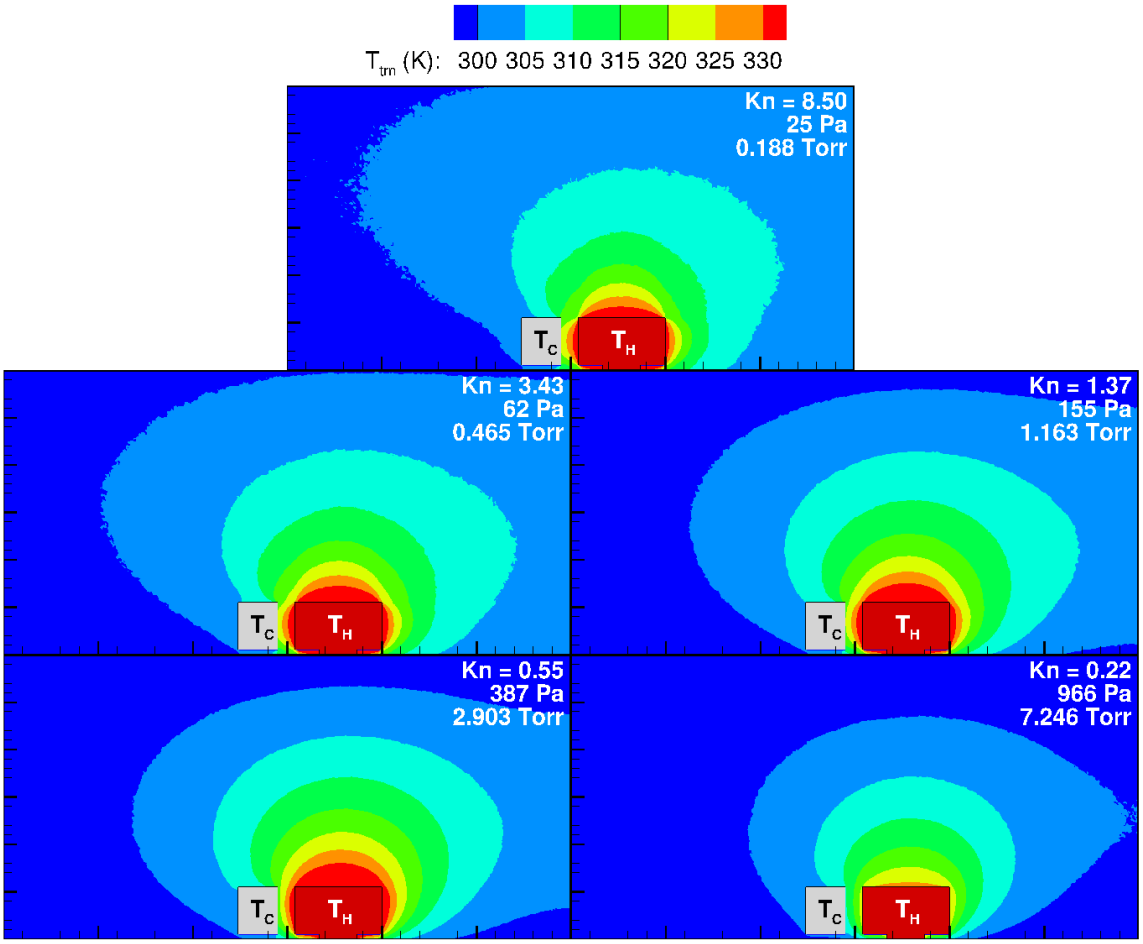

A. 4.: Temperature flowfield of MIKRA Gen2 for all five pressures with 50% N2 and 50% H2O.